SMAI-JCM
SMAI Journal of Computational Mathematics

A two-dimensional method for a family of dispersive shallow water models

Nora Aïssiouene, Marie-Odile Bristeau, Edwige Godlewski, Anne Mangeney, Carlos Parés Madroñal & Jacques Sainte-Marie

Volume 6 (2020), p. 187-226.

<http://smai-jcm.centre-mersenne.org/item?id=SMAI-JCM_2020__6__187_0>

SMAI Journal of Computational Mathematics
Vol. 6, 187-226 (2020)

A two-dimensional method for a family of dispersive shallow water models

Nora Aïssiouene [1]
Marie-Odile Bristeau [2]
Edwige Godlewski [3]
Anne Mangeney [4]
Carlos Parés Madroñal [5]
Jacques Sainte-Marie [6]

[1] Sorbonne Université, Institut Carnot Smiles, 4 Place Jussieu, F-75252 Paris cedex 05
E-mail address: Nora.Aissiouene@upmc.fr
[2] Inria Paris, 2 rue Simone Iff, CS 42112, 75589 Paris Cedex 12, France & Sorbonne Université, Université de Paris, CNRS, Laboratoire Jacques-Louis Lions, LJLL, F-75005 Paris
E-mail address: Marie-Odile.Bristeau@inria.fr
[3] Inria Paris, 2 rue Simone Iff, CS 42112, 75589 Paris Cedex 12, France & Sorbonne Université, Université de Paris, CNRS, Laboratoire Jacques-Louis Lions, LJLL, F-75005 Paris
E-mail address: Edwige.Godlewski@upmc.fr
[4] Univ. de Paris, Institut de Physique du Globe de Paris, Seismology Group, 1 rue Jussieu, Paris F-75005, France
E-mail address: Anne.Mangeney@ipgp.fr
[5] EDANYA, Universidad de Málaga, Campus de Teatinos s/n, 29080 Málaga, Spain
E-mail address: pares@uma.es
[6] Inria Paris, 2 rue Simone Iff, CS 42112, 75589 Paris Cedex 12, France & Sorbonne Université, Université de Paris, CNRS, Laboratoire Jacques-Louis Lions, LJLL, F-75005 Paris
E-mail address: Jacques.Sainte-Marie@inria.fr.

Abstract. We propose a numerical method for a family of two-dimensional dispersive shallow water systems with topography. The considered models consist in shallow water approximations – without the hydrostatic assumption – of the incompressible Euler system with free surface. Hence, the studied models appear as extensions of the classical shallow water system enriched with dispersive terms. The model formulation motivates us to use a prediction-correction scheme for its numerical approximation. The prediction part leads to solving a classical shallow water system with topography while the correction part leads to solving an elliptic-type problem. The numerical approximation of the considered dispersive models in the two-dimensional case over unstructured meshes is described, it requires to combine finite volume and finite element techniques. A special emphasis is given to the formulation and the numerical resolution of the correction step (variational formulation, inf-sup condition, boundary conditions,...). The numerical procedure is confronted with analytical and experimental test cases. Finally, an application to a real tsunami case is given.

2020 Mathematics Subject Classification. 65M12, 74S10, 76M12, 35L65, 35Q30, 35Q35, 76D05.

Keywords. shallow water flows, dispersive effects, prediction-correction scheme, combined finite volume / finite element technique, dispersive wave propagation, tsunami propagation.

1. Introduction

Mathematical models for free surface flows are widely studied but their analysis and numerical approximation remain a challenging issue. The incompressible Navier-Stokes system with free surface being very difficult to study, it is often replaced by the classical shallow water equations [9]. But these equations rely on the hydrostatic assumption, hence when the vertical acceleration of the fluid can no longer be neglected, the shallow water system fails to represent dispersive effects e.g. in the context of wave propagation [36, 11].

Many shallow water type models taking into consideration the dispersive effects are available, see [38, 13, 12, 51, 50, 22, 21], the list being non-exhaustive. In this paper, we introduce a family of dispersive models depending on a parameter and where only first order derivatives appear. For a given value of the parameter we obtain the dispersive model proposed by some of the authors [21, 2] and for another value of the parameter the studied model corresponds to the Green-Naghdi model [38, 4, 14, 23, 28] up to some small error terms involving the bathymetry gradient.

The non linear shallow water model with topography is an hyperbolic system with source term, which has been extensively studied and the literature provides efficient algorithms for this model, see [18, 48, 49] for analysis results and [37, 47, 17, 6, 7] for numerical methods. Since non-hydrostatic models are no longer hyperbolic, it is necessary to propose new numerical algorithms and there is a strong need for methods able to capture dispersion with a good accuracy and able to deal with real situations. Several approaches have been proposed to solve these models, especially in one dimension or in two dimensions with a structured grid (see [25, 14, 23, 31, 46]). A discretization with a discontinuous Galerkin method has been proposed in [28] to treat the dispersive part, and more recently, A. Duran and F. Marche designed an hybrid method [29] for the two-dimensional Green-Naghdi model. The same model is considered in [33] with a combined finite volume / finite element method on unstructured meshes for its numerical approximation. In [34], the authors use a contravariant formulation of the model and a high order WENO discretization scheme.

Compared to most of existing techniques where the non-hydrostatic part of the pressure is eliminated – leading to third order derivative terms – we consider a formulation with only first order derivatives as initially proposed in [21]. This strategy leads to a non-hydrostatic pressure governed by an elliptic type equation as in the Chorin-Teman decomposition technique applied for the classical incompressible Euler system [53]. More precisely, the elliptic part of the system has the form of a Sturm-Liouville type equation and admits several formulations depending on the boundary conditions to be applied. A similar approach is used in [33] but the numerical analysis of the correction step, especially the study of the $inf - sup$ condition – that is important e.g. for the treatment of wet/dry interfaces – is not carried out.

The aim of this paper is to provide, for this family of two-dimensional dispersive models, a stable and robust numerical method coupling finite volume and finite element strategies and able to simulate real cases where the topography can be complex. Therefore, the space discretization is performed over unstructured meshes.

The strong points of the paper are

- a model formulation with only first order derivatives and with a duality relation between the pressure gradient and the divergence free condition similar to the one available for the classical incompressible Euler system,
- the numerical analysis of the elliptic equations governing the non-hydrostatic pressure (inf-sup condition),
- a numerical scheme able to deal with wet/dry interfaces,
- the numerical treatment of the boundary conditions facilitated by the model structure and the time splitting,
- the convergence order of the method evaluated using several analytical solutions,
- the numerical procedure confronted with several test cases of wave propagation including a tsunami propagation.

It is important to notice that the computational costs coming from the resolution of the elliptic equation can be very large and, when considering fine meshes (see paragraph 6.4), a preconditioning of the system is required. This aspect is not in the scope of this paper.

The paper is organized as follows. In the next section, we present the family of dispersive models and its justification from the full Euler system. Section 3 is devoted to the formulation of the Chorin-Temam approach (prediction-correction scheme) in the studied context, we mainly focus on the correction step consisting in the resolution of a mixed problem (velocity-pressure). In Section 4, we propose two approximation spaces (P_1/P_1 and P_1-isoP_2/P_1) for the finite element scheme applied to the mixed problem. In Section 5, details about the complete numerical scheme are given. Finally in Section 6, we validate the approach using comparisons with analytical solutions and experimental data, and then we apply the numerical scheme to an earthquake generated tsunami and compare the simulation results to field measurements.

2. A class of dispersive models

In this section, the family of 2d shallow water dispersive models studied in this paper is presented. First its formulation where only first order derivatives appear is given, it corresponds to an extension to the 2d case of previous works of some of the authors [21]. Then we propose a justification of the family of models by the means of a depth averaging of the incompressible Euler system with free surface and a suitable choice for the velocity and pressure fields. Finally a rewriting of the model, more suitable for numerical approximation, is presented.

2.1. Model formulation

We consider the family of 2d shallow water dispersive models written under the form

$$\frac{\partial H}{\partial t} + \frac{\partial (Hu)}{\partial x} + \frac{\partial (Hv)}{\partial y} = 0, \tag{2.1}$$

$$\frac{\partial (Hu)}{\partial t} + \frac{\partial}{\partial x}\left(Hu^2 + \frac{g}{2}H^2 + Hp\right) + \frac{\partial (Huv)}{\partial y} = -(gH + \delta p)\frac{\partial z_b}{\partial x}, \tag{2.2}$$

$$\frac{\partial (Hv)}{\partial t} + \frac{\partial (Huv)}{\partial x} + \frac{\partial}{\partial y}\left(Hv^2 + \frac{g}{2}H^2 + Hp\right) = -(gH + \delta p)\frac{\partial z_b}{\partial y}, \tag{2.3}$$

$$\frac{\partial (Hw)}{\partial t} + \frac{\partial (Huw)}{\partial x} + \frac{\partial (Hvw)}{\partial y} = \delta p, \tag{2.4}$$

$$2w = -H\frac{\partial u}{\partial x} + \delta u\frac{\partial z_b}{\partial x} - H\frac{\partial v}{\partial y} + \delta v\frac{\partial z_b}{\partial y}, \tag{2.5}$$

where $\mathbf{u} = (u, v, w)^T$ is the velocity of the fluid, p is the non-hydrostatic part of the fluid pressure, the total pressure is given by $p_{tot} = gH/2 + p$ and g represents the gravity acceleration; $\delta \in \mathbb{R}$ is a parameter, its value will be discussed below especially in paragraph 2.3.

We consider that the model (2.1)-(2.5) is written for a two-dimensional domain $\Omega \subset \mathbb{R}^2$ delimited by the boundary $\Gamma = \Gamma_{in} \cup \Gamma_{out} \cup \Gamma_s$ as described in Fig. 2.1-*(a)*. We denote $\mathbf{x} = (x, y)$. The topography profile is $z_b(\mathbf{x})$ and the free surface is defined by

$$\eta(\mathbf{x}, t) := H(\mathbf{x}, t) + z_b(\mathbf{x}), \tag{2.6}$$

where $H(\mathbf{x}, t)$ is the water depth, see Fig. 2.1-*(b)*.

For smooth solutions, the system (2.1)-(2.5) satisfies the following energy balance

$$\frac{\partial E}{\partial t} + \nabla_0 . \Big(\mathbf{u}(E + \frac{g}{2}H^2 + Hp)\Big) = 0, \tag{2.7}$$

with $E = H(u^2 + v^2 + 2w^2/\delta)/2 + g(\eta^2 - z_b^2)/2$ and the operator $\nabla_0 = (\frac{\partial}{\partial x}, \frac{\partial}{\partial y}, 0)^T$.

Compared to the classical formulation of the Green-Naghdi system, the formulation (2.1)-(2.5) has two main advantages:

- the writing of the model exhibits a structure that is very similar to the full incompressible Euler system with free surface. Hence, Eq. (2.1) stands for the mass conservation, Eqs. (2.2)-(2.4) are a vertically averaged version of the momentum equations along x, y and z of the full Euler system and Eq. (2.5) is a shallow water version of the divergence free condition. These similarities allow to adapt for the dispersive shallow water model numerical techniques initially proposed for the full Euler system.
- The system (2.1)-(2.5) contains only first order derivatives and their numerical treatment is easier than third order derivatives appearing in most of the dispersive shallow water models studied in the literature (Peregrine [51], Nwogu [50], BBM [12], Green-Naghdi [38]...).

2.2. **The boundary conditions**

The set of equations (2.1)-(2.5) is completed with the following boundary conditions. We are considering a channel with an inlet Γ_{in} and an outlet Γ_{out} and we impose specific conditions on each of them. The inflow is imposed by a given discharge $\mathbf{q}_g$ on Γ_{in}, and a water depth h_g is imposed on Γ_{out}. Finally, we prescribe slip boundary conditions for the velocity at the walls of the channel Γ_s. Hence we have

$$H\mathbf{u}(\mathbf{x}, t) = \mathbf{q}_g(\mathbf{x}, t), \quad \text{on } \Gamma_{in}, \tag{2.8}$$

$$H(\mathbf{x}, t) = h_g(\mathbf{x}, t), \quad \text{on } \Gamma_{out}, \tag{2.9}$$

$$\mathbf{u}(\mathbf{x}, t) \cdot \mathbf{n} = 0, \quad \text{on } \Gamma_s. \tag{2.10}$$

Notice that we can replace the prescribed water depth at the outflow by a free outflow consisting in imposing a Neumann boundary condition over the elevation

$$\nabla_0 H \cdot \mathbf{n} = 0, \quad \text{on } \Gamma_{out},$$

where the vector $\mathbf{n} = (n_x, n_y, 0)^T$ is the outward unit normal vector to the boundary Γ, see Fig. 2.1.

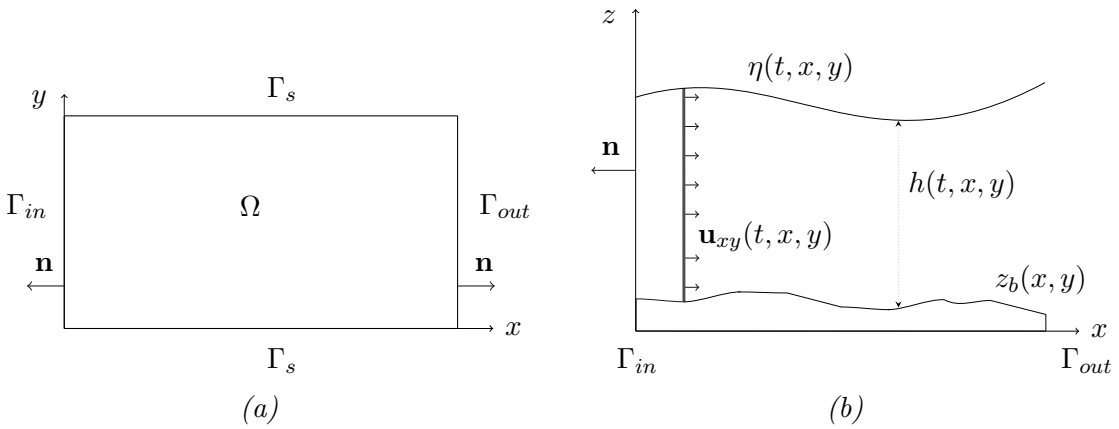

FIGURE 2.1. Model domain and notations, *(a)* view from above and *(b)* vertical cross section, $\mathbf{u}_{xy}$ is the horizontal part of the velocity vector i.e. $\mathbf{u}_{xy} = (u, v)^T$.

2.3. **A justification of the model**

In this paragraph, we propose a unified approach consisting in an approximation of the depth averaged Euler system and allowing to recover various dispersive shallow water models, see especially paragraph 2.3.2 and remark 2.5. But it is important to notice that the approximation process of the Euler system we propose is an *a posteriori* justification of the model (2.1)-(2.5) and cannot be considered as a modeling strategy.

2.3.1. *The Euler system*

The three-dimensional incompressible Euler system describing a free surface gravitational flow moving over a bottom topography $z_b(\mathbf{x})$ writes

$$\nabla.\mathbf{V} = 0, \tag{2.11}$$

$$\frac{\partial \mathbf{V}}{\partial t} + \nabla.(\mathbf{V} \otimes \mathbf{V}) + \nabla \tilde{p} = -\mathbf{g}, \tag{2.12}$$

where $\mathbf{V} = (u_1, u_2, u_3)^T$ is the velocity, $\tilde{p}$ is the fluid pressure and $\mathbf{g} = (0, 0, g)^T$ represents the gravity forces. The operator ∇ denotes $\nabla = \left(\frac{\partial}{\partial x}, \frac{\partial}{\partial y}, \frac{\partial}{\partial z}\right)^T$.

Since we consider a free surface flow, the definition (2.6) and the system (2.11)-(2.12) is completed with the following boundary conditions. At the free surface, the kinematic boundary condition is

$$\frac{\partial \eta}{\partial t} + u_{1,s}\frac{\partial \eta}{\partial x} + u_{2,s}\frac{\partial \eta}{\partial y} - u_{3,s} = 0, \tag{2.13}$$

whereas at the bottom we have the non-penetration condition

$$u_{1,b}\frac{\partial z_b}{\partial x} + u_{2,b}\frac{\partial z_b}{\partial y} - u_{3,b} = 0, \tag{2.14}$$

where the subscript s (resp. b) denotes the value of the considered quantity at the free surface (resp. at the bottom).

The dynamic boundary condition at the free surface is given by

$$\tilde{p}_s = \tilde{p}(\mathbf{x}, \eta(\mathbf{x}, t), t) = p^a(\mathbf{x}, t), \tag{2.15}$$

where p^a is given and mimics the role of the atmospheric pressure. Throughout this paper, we assume $p^a(\mathbf{x}, t) = p_0^a = cst$.

For the incompressible Euler system (2.11)-(2.12), a crucial point is the duality relation between the gradient and divergence operators which writes

$$\int_{\Omega\times[z_b,\eta]} \tilde{p}\nabla.\mathbf{V} d\mathbf{x}dz = \int_{\partial(\Omega\times[z_b,\eta])} \tilde{p}\mathbf{V}.\mathbf{n}ds - \int_{\Omega\times[z_b,\eta]} \mathbf{V}.\nabla\tilde{p}d\mathbf{x}dz. \tag{2.16}$$

Notice that in Eq. (2.16), $\mathbf{n}$ is the unit outward normal to the domain $\Omega \times [z_b, \eta]$.

2.3.2. *An approximation of the Euler system*

For free surface flows, the vertical direction plays a particular role since it corresponds to the direction of the gravity. Moreover the fluid domain, in our case, is thin in this direction. It is easy to see (cf. [35, Lemma 2.1]) that a depth averaging of the Euler system (2.11)-(2.12) completed with the boundary

conditions (2.13)-(2.15) leads to

$$\frac{\partial H}{\partial t} + \nabla_{x,y}. \int_{z_b}^{\eta} \mathbf{v} dz = 0, \tag{2.17}$$

$$\frac{\partial}{\partial t} \int_{z_b}^{\eta} \mathbf{v} dz + \nabla_{x,y}. \int_{z_b}^{\eta} \mathbf{v} \otimes \mathbf{v} dz + \nabla_{x,y} \int_{z_b}^{\eta} \tilde{p} dz = \tilde{p}(\mathbf{x}, z_b(\mathbf{x}), t) \nabla_{x,y} z_b, \tag{2.18}$$

$$\frac{\partial}{\partial t} \int_{z_b}^{\eta} u_3 dz + \nabla_{x,y}. \int_{z_b}^{\eta} u_3 \mathbf{v} dz = \tilde{p}(\mathbf{x}, z_b(\mathbf{x}), t) - gH, \tag{2.19}$$

with $\mathbf{v} = (u_1, u_2)$ and $\nabla_{x,y} = (\frac{\partial}{\partial x}, \frac{\partial}{\partial y})^T$, completed with (2.11).

And the following proposition holds.

Proposition 2.1. *The model* (2.1)-(2.5) *is obtained by a depth averaging of the incompressible Euler system with free surface* (2.11)-(2.15) *completed with the following assumption concerning the variations along the vertical axis of the velocity field* $\mathbf{V}$ *and of the pressure* $\tilde{p}$

$$u_1(\mathbf{x}, z, t) = u(\mathbf{x}, t), \quad u_2(\mathbf{x}, z, t) = v(\mathbf{x}, t), \tag{2.20}$$

$$u_3(\mathbf{x}, z, t) = \varphi_\delta \left(\frac{\eta - z}{H} \right) w(\mathbf{x}, t), \tag{2.21}$$

$$\tilde{p}(\mathbf{x}, z, t) = p_0^a + g(\eta - z) + \psi_\delta \left(\frac{\eta - z}{H} \right) p(\mathbf{x}, t), \tag{2.22}$$

where the two families of real valued functions $\psi_\delta = \psi_\delta(z)$ *and* $\varphi_\delta = \varphi_\delta(z)$ *satisfy*

$$\begin{cases} \int_0^1 \psi_\delta(z) dz = \int_0^1 \varphi_\delta(z) dz = \frac{1}{2} \int_0^1 \varphi_\delta(z) \psi_\delta'(z) dz = \varphi_\delta(1) = 1, \\ \psi_\delta(1) = \delta, \\ \psi_\delta(0) = 0. \end{cases} \tag{2.23}$$

Proof. [Proof of prop. 2.1] In order to be consistent with the shallow water assumption, the choice (2.20) is natural since it consists in assimilating the horizontal velocity field with its vertical mean. It remains to justify the approximations for the velocity u_3 and for the pressure $\tilde{p}$. The chosen expression (2.22) means that $\psi_\delta((\eta - z)/H) p(\mathbf{x}, t)$ corresponds to the non-hydrostatic part of the pressure. Obviously, Eq. (2.17) with the choice (2.20) gives (2.1). Likewise Eq. (2.2) is derived from Eq. (2.18) with the choices (2.20),(2.22) using the constraints (2.23). Notice that the definition (2.22) coupled with (2.23) implies that the boundary condition (2.15) is satisfied. Equation (2.4) is obtained from Eq. (2.19) using the definitions (2.20),(2.21),(2.22) and the constraints (2.23).
The duality relation (2.16) is a guideline for the definition of the shallow water version of the divergence free condition (2.11). Using expression (2.22), the left hand side of (2.16) involving the non-hydrostatic part of the pressure becomes

$$\int_{\Omega \times [z_b, \eta]} p \psi_\delta \left(\frac{\eta - z}{H} \right) \nabla.\mathbf{V} d\mathbf{x} dz = \int_\Omega p \left(\int_{z_b}^{\eta} \psi_\delta \left(\frac{\eta - z}{H} \right) \nabla.\mathbf{V} dz \right) d\mathbf{x},$$

and using (2.11),(2.14),(2.20),(2.21),(2.23), we remark that

$$\begin{aligned} 0 = \int_{z_b}^{\eta} \psi_\delta \left(\frac{\eta - z}{H} \right) \nabla.\mathbf{V} dz = \int_{z_b}^{\eta} \psi_\delta \left(\frac{\eta - z}{H} \right) \frac{\partial u}{\partial x} dz + \int_{z_b}^{\eta} \psi_\delta \left(\frac{\eta - z}{H} \right) \frac{\partial v}{\partial y} dz \\ + \left[u_3 \psi_\delta \left(\frac{\eta - z}{H} \right) \right]_{z_b}^{\eta} - \int_{z_b}^{\eta} w \varphi_\delta \left(\frac{\eta - z}{H} \right) \frac{\partial}{\partial z} \psi_\delta \left(\frac{\eta - z}{H} \right) dz, \end{aligned}$$

leading to Eq. (2.5), which completes the proof. ∎

Among all the possible choices for ψ_δ and φ_δ, we exhibit two possible choices for ψ_δ, namely

$$\psi_\delta^1(z) = 3(\delta-2)z^2 + 2(3-\delta)z \quad \text{for } \delta \in \mathbb{R},$$
$$\psi_\delta^2(z) = \delta z^{\delta-1}, \quad \text{for } \delta \geq 1,$$

and for φ_δ, possible choices are $\varphi_\delta^i(z) = \frac{2}{\delta} + 1 - \frac{2}{\delta}\psi_\delta^i(z)$ with $i = 1, 2$. Figure 2.2 illustrates the shape of the functions ψ_δ and φ_δ for two typical values of δ namely $\delta = 2$ (corresponding to advection dominated flows) and $\delta = 3/2$ (adapted to a wave propagation phenomenon). It appears that the functions ψ_δ and φ_δ do not significantly differ when $\delta = 2$ or when $\delta = 3/2$, the choice $\delta = 2$ corresponding to a linear profile. Notice that for $\delta = 2$, $\psi_2^1(z) = \psi_2^2(z)$ and $\varphi_2^1(z) = \varphi_2^2(z)$.

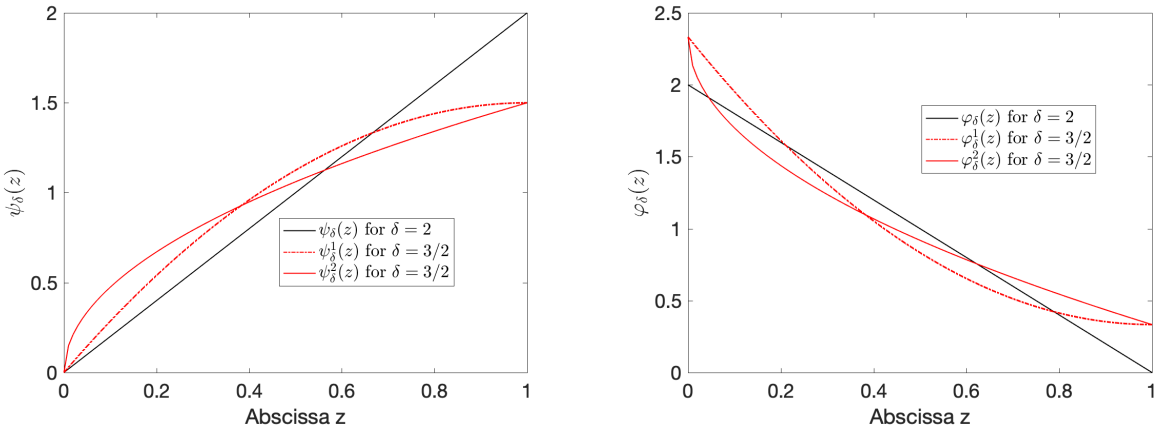

FIGURE 2.2. Shape of the functions ψ_δ and φ_δ for two typical values of δ. Notice that $z = 0$ corresponds to the free surface and $z = 1$ to the bottom.

Remark 2.2. Instead of considering the approximation (2.20) where the horizontal velocity is supposed to be constant along the vertical axis, a piecewise constant approximation along the vertical axis can be considered (see [32]), leading to another set of 2d equations approximating the 3d Euler system with free surface.

2.4. **Rewriting of the model**

2.4.1. *New formulation*

We now propose a modified formulation of the model (2.1)-(2.5), resulting from a simple change of variable. The two formulations are obviously equivalent, whatever the given formulation.

A simple change of variable, namely $w = \gamma\hat{w}/2$ with $\gamma^2 = 2\delta$, in the system (2.1)-(2.5) leads to the model

$$\frac{\partial H}{\partial t} + \frac{\partial (Hu)}{\partial x} + \frac{\partial (Hv)}{\partial y} = 0, \tag{2.24}$$

$$\frac{\partial (Hu)}{\partial t} + \frac{\partial}{\partial x}\left(Hu^2 + \frac{g}{2}H^2 + Hp\right) + \frac{\partial (Huv)}{\partial y} = -(gH + \frac{\gamma^2}{2}p)\frac{\partial z_b}{\partial x}, \tag{2.25}$$

$$\frac{\partial (Hv)}{\partial t} + \frac{\partial (Huv)}{\partial x} + \frac{\partial}{\partial y}\left(Hv^2 + \frac{g}{2}H^2 + Hp\right) = -(gH + \frac{\gamma^2}{2}p)\frac{\partial z_b}{\partial y}, \tag{2.26}$$

$$\frac{\partial (Hw)}{\partial t} + \frac{\partial (Huw)}{\partial x} + \frac{\partial (Hvw)}{\partial y} = \gamma p, \tag{2.27}$$

$$\gamma w = -H\frac{\partial u}{\partial x} + \frac{\gamma^2}{2}u\frac{\partial z_b}{\partial x} - H\frac{\partial v}{\partial y} + \frac{\gamma^2}{2}v\frac{\partial z_b}{\partial y}, \tag{2.28}$$

where the $\hat{}$ for the variable w has been omitted. The system (2.24)-(2.28) defines a family $\{\mathcal{M}_\gamma\}$ of dispersive models written in the more condensed form

$$\frac{\partial H}{\partial t} + \nabla_0 \cdot (H\mathbf{u}) = 0, \tag{2.29}$$

$$\frac{\partial (H\mathbf{u})}{\partial t} + \nabla_0 \cdot (H\mathbf{u} \otimes \mathbf{u}) + \nabla_0(\frac{g}{2}H^2) + \nabla_{sw}^\gamma p = -gH\nabla_0(z_b), \tag{2.30}$$

$$\mathrm{div}_{sw}^\gamma(\mathbf{u}) = 0, \tag{2.31}$$

where the shallow water versions of the gradient and divergence operators are defined by

$$\nabla_{sw}^\gamma f = \begin{pmatrix} H\frac{\partial f}{\partial x} + f\frac{\partial \zeta}{\partial x} \\ H\frac{\partial f}{\partial y} + f\frac{\partial \zeta}{\partial y} \\ -\gamma f \end{pmatrix}, \tag{2.32}$$

$$\mathrm{div}_{sw}^\gamma(\mathbf{w}) = \frac{\partial (Hw_1)}{\partial x} + \frac{\partial (Hw_2)}{\partial y} - w_1\frac{\partial \zeta}{\partial x} - w_2\frac{\partial \zeta}{\partial y} + \gamma w_3, \tag{2.33}$$

for $\mathbf{w} = (w_1, w_2, w_3)^T$ and

$$\zeta = H + \frac{\gamma^2}{2}z_b. \tag{2.34}$$

Whereas ζ depends on γ, for the sake of simplicity, we have adopted a simplified notation and ζ_γ is replaced by ζ.

The following proposition holds.

Proposition 2.3. *Whatever the value of γ, the operators div_{sw}^γ and ∇_{sw}^γ satisfy the duality relation*

$$\int_\Omega \nabla_{sw}^\gamma(f) \cdot \mathbf{w} d\mathbf{x} = -\int_\Omega \mathrm{div}_{sw}^\gamma(\mathbf{w}) f d\mathbf{x} + \int_\Gamma H f \mathbf{w} \cdot \mathbf{n} ds. \tag{2.35}$$

In Eq. (2.35), f and $\mathbf{w}$ belong to suitable function spaces that will be precised later.

The duality relation (2.35) between the gradient and divergence operator is analogous to relation (2.16) for the full incompressible Euler system. The property (2.35) is crucial for the method presented in the following since we will consider a mixed formulation of the discrete problem in velocity/pressure (see Section 3.4), which will lead to having an operator for the pressure and its adjoint for the velocity.

Remark 2.4. It is important to point out that in the model (2.1)-(2.5), it is not possible to define a shallow water version of the gradient and divergence operators satisfying a duality relation analogous

to (2.35) unless $\delta = 2$ (corresponding to $\gamma = 2$ in (2.35)) in which case the models (2.1)-(2.5) and (2.24)-(2.28) coincide.

2.4.2. *The value of* γ

Dispersive models are often obtained using an asymptotic expansion of the Euler or Navier-Stokes system coupled with physical assumptions concerning the hydrodynamic regime. For shallow water flows, dispersive models are extensions of the classical shallow water system [35].

Particular choices of the parameter γ correspond to two dispersive models studied in the literature. More precisely, $\gamma = \sqrt{3}$ leads to the Green-Naghdi model [38] whereas $\gamma = 2$ leads to the model described in [21]. The complexity of the Euler system, able to represent many regimes from wave propagation to advection dominated flows, explains why many dispersive shallow water models have been proposed, see the references given in Section 1.

For $\gamma = \sqrt{3}$, the model (2.24)-(2.28) – or equivalently for $\delta = 3/2$, the model (2.1)-(2.5) – corresponds, up to small error terms, to the Green-Naghdi model [38] studied e.g. in [15, 44], this equivalence is proved in Appendix A. In the context of wave propagation i.e. with flat bottom and assuming the water depth has the form $H = H_0 + f(kx - \omega t)$ with $H_0 = cst$ and $|f(.)| \ll H_0$, it is easy to see that the linear dispersion relation of the model $\mathcal{M}_\gamma$ is given by

$$\frac{\omega}{k} = \sqrt{gH_0}\left(1 + \frac{(kH_0)^2}{\gamma^2}\right)^{-1/2},$$

corresponding for $\gamma = \sqrt{3}$ in the context of large wavelength ($kH_0 \ll 1$) and up to $\mathcal{O}((kH_0)^4)$ terms, to the classical Airy wave dispersion relation [1].

The choice $\gamma = 2$ corresponds to the model proposed and studied in 1d by some of the authors in [21, 2]. The model $\mathcal{M}_2$ is more adapted to advection dominated flows. Indeed we can exhibit analytical solutions for the full Euler system that are also solutions of the model $\mathcal{M}_\gamma$ only for $\gamma = 2$, see remark 6.2. Thus the model $\mathcal{M}_2$ shares common analytical solutions with the full Euler system.

But for the numerical analysis part that is the core of this paper, it is not necessary to single out one value of γ or another since the proposed framework is valid for the whole family of models.

Remark 2.5. Notice that some approximations and/or linearizations in the dispersive terms of $\mathcal{M}_\gamma$ allow to recover other dispersive models such as Peregrine's model [51].

Indeed, considering a linearized version of $\mathcal{M}_{\sqrt{3}}$ (where $H = H_0 + h$, $H_0 = cst$, $h \ll H_0$, $uv \ll 1$, $uw \ll 1$) and a flat bottom gives

$$\frac{\partial H}{\partial t} + \frac{\partial (Hu)}{\partial x} + \frac{\partial (Hv)}{\partial y} = 0, \tag{2.36}$$

$$\frac{\partial u}{\partial t} + u\frac{\partial u}{\partial x} + v\frac{\partial u}{\partial y} + g\frac{\partial H}{\partial x} + \frac{\partial p}{\partial x} = 0, \tag{2.37}$$

$$\frac{\partial v}{\partial t} + u\frac{\partial v}{\partial x} + v\frac{\partial v}{\partial y} + g\frac{\partial H}{\partial y} + \frac{\partial p}{\partial y} = 0, \tag{2.38}$$

$$H_0\frac{\partial w}{\partial t} = \sqrt{3}p, \tag{2.39}$$

$$\sqrt{3}w = -H_0\frac{\partial u}{\partial x} - H_0\frac{\partial v}{\partial y}. \tag{2.40}$$

Then, substituting Eq. (2.40) in Eq. (2.39) gives the expression of the pressure p. And inserting the obtained expression for p in Eqs.(2.37),(2.38) gives the Peregrine model [51].

3. Time and space discretizations

This section is devoted to the numerical approximation of the dispersive model given by (2.29)-(2.31).

The main ingredient of the numerical strategy consists in a time splitting based on a Chorin-Temam projection-correction scheme (see [24, 53, 39, 40]). The time discretization is first presented then the space discretizations are detailed in paragraphs 3.2,3.3 and 3.4 of this section.

3.1. Prediction - correction scheme

The prediction-correction method, widely used to approximate the Navier-Stokes equations and based on a time-splitting scheme, is applied to the problem (2.29)-(2.31). At each time step, the problem is decomposed into two steps. In the first one, we solve the hyperbolic part leading to a predicted state which does not satisfy the divergence free constraint. During the second step, we update the predicted state so that the divergence free constraint (2.31) is satisfied.

Let us introduce the notations

$$X = \begin{pmatrix} H \\ Hu \\ Hv \\ Hw \end{pmatrix}, \quad F(X) = \begin{pmatrix} Hu & Hv \\ Hu^2 + \frac{g}{2}H^2 & Huv \\ Huv & Hv^2 + \frac{g}{2}H^2 \\ Huw & Hvw \end{pmatrix}, \quad S(X) = \begin{pmatrix} 0 \\ -gH\frac{\partial z_b}{\partial x} \\ -gH\frac{\partial z_b}{\partial y} \\ 0 \end{pmatrix}, \quad R = \begin{pmatrix} 0 \\ \nabla_{sw}^{\gamma} p \end{pmatrix}.$$

Then, the system (2.29)-(2.31) can be written under the form

$$\begin{aligned} &\frac{\partial X}{\partial t} + \nabla_{x,y} \cdot F(X) + R = S(X), \\ &\mathrm{div}_{sw}^{\gamma}(\mathbf{u}) = 0. \end{aligned}$$

We set t^0 the initial time and $t^{n+1} = t^n + \Delta t^n$ where Δt^n satisfies a stability condition (CFL) precised later, the state X^n will denote an approximation of $X(t^n)$. For each time step, we consider an intermediate state which will be denoted with the superscript $^{n+1/2}$. So the first step leads to solving the hyperbolic system with the topography source term – that is exactly the classical shallow water system – in order to get the state $X^{n+1/2} = (H^{n+1/2}, (Hu)^{n+1/2}, (Hv)^{n+1/2}, (Hw)^{n+1/2})^T$. The semi-discretization in time can be summarized in the following steps

$$X^{n+1/2} = X^n - \Delta t^n \nabla_{x,y}.F(X^n) + \Delta t^n S(X^n), \tag{3.1}$$

$$X^{n+1} = X^{n+1/2} - \Delta t^n R^{n+1}, \tag{3.2}$$

$$\mathrm{div}_{sw}^{\gamma}\, \mathbf{u}^{n+1} = 0. \tag{3.3}$$

The equation (3.2) allows us to correct the predicted value $X^{n+1/2}$ in order to obtain a state which satisfies the divergence free condition (3.3). The equation satisfied by the pressure is then an elliptic equation which is obtained by applying the shallow water divergence operator $\mathrm{div}_{sw}^{\gamma}$ to Eq. (3.2) and reads

$$\mathrm{div}_{sw}^{\gamma}\left(\frac{\nabla_{sw}^{\gamma}\, p^{n+1}}{H^{n+1}}\right) = \frac{1}{\Delta t^n}\mathrm{div}_{sw}^{\gamma}\left(\frac{(H\mathbf{u})^{n+1/2}}{H^{n+1/2}}\right). \tag{3.4}$$

Once the pressure has been determined by the elliptic equation (3.4), the correction step (3.2) gives the final step X^{n+1}.

Remark 3.1. For the initial conditions, at time t^0, the initial state X^0 is prescribed. Since the pressure is obtained from (3.4), it is not necessary to impose any initial condition for the pressure.

In this paper, we briefly describe the step (3.1) in paragraph 3.3 but we will focus on the second step of the scheme, namely Eqs. (3.2)-(3.3) discretized by a finite element method. Therefore, we will consider the state $X^{n+1/2}$ as a given state and the state X^{n+1} as the unknown. The operator $\mathrm{div}_{sw}^{\gamma}\left(\frac{\nabla_{sw}^{\gamma}}{H}\right)$ is a shallow water version of the Laplacian operator and is denoted by Δ_{sw}^{γ}, using (2.32),(2.33) its expression is given by

$$\Delta_{sw}^{\gamma}\ p = \nabla_{x,y}.(H\nabla_{x,y}p) + \left(\Delta_{x,y}\zeta - \frac{1}{H}\left(\left(\frac{\partial\zeta}{\partial x}\right)^2 + \left(\frac{\partial\zeta}{\partial y}\right)^2 + \gamma^2\right)\right)p, \tag{3.5}$$

with $\Delta_{x,y}f = \nabla_{x,y}.(\nabla_{x,y}f)$ and ζ defined by (2.34). Therefore, the operator Δ_{sw}^{γ} can be written under the form of a Sturm-Liouville operator.

3.2. **Space discretization**

Concerning the space discretization, each step – prediction step and correction step – is solved with its own scheme. The method relies on a combination between a finite volume scheme for the hyperbolic part (3.1) and a finite element scheme for the elliptic part (3.2)-(3.3). The idea is to start with a primal mesh which is triangular, then a dual mesh is built by the finite volume cells centered on the vertices.

Let us consider Ω the computational domain with boundary Γ, which is assumed to be polygonal. Let $\mathcal{T}$ be a triangulation of Ω. We denote by S_h the set of the vertices of the mesh

$$S_h = \{s_i = (x_i, y_i) \in \mathcal{T}\}. \tag{3.6}$$

We recall here the general formalism of finite volumes on unstructured meshes, and the finite element method we use for the correction part will be detailed in Section 4.
Let us define the finite volume cell C_i associated to the vertex s_i. The cells C_i are built by joining the centers of mass of the triangles surrounding each vertex s_i. We use the following notations (see Figure 3.1)

- $|C_i|$, area of C_i,
- Γ_{ij}, boundary edge between the cells C_i and C_j,
- L_{ij}, length of Γ_{ij},
- $\mathbf{n}_{ij}$, unit normal to Γ_{ij}, outward to C_i ($\mathbf{n}_{ji} = -\mathbf{n}_{ij}$),
- $\mathcal{K}_i$ the set of nodes connected to the node s_i.

Remark 3.2. The variables $H, H\mathbf{u}$ are estimated first as constant mean values on the cells C_i by the finite volume scheme, which gives the intermediate state $X^{n+1/2}$. For the finite element scheme, the state X^{n+1} is approximated at the vertices of the triangles, and for the required value of $X^{n+1/2}$ at the node s_i, we use the constant mean value computed on the cell C_i. Similarly, for the finite volume step, the required mean value X^{n+1} at cell C_i is given by the value at node s_i. Therefore, combining the finite volume and the finite element approximations, we will denote by X_i both the constant mean value on cell C_i and the value at node s_i.

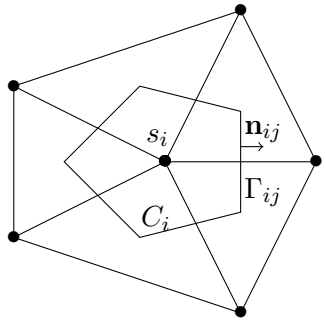

FIGURE 3.1. Representation of the dual mesh

3.3. **Finite volume scheme for the prediction part**

We denote by X_i^n the approximation of $X(t^n)$ on a finite volume cell C_i, the state X_i^n is the approximation of the cell average of $X(\mathbf{x}, t^n)$

$$X_i^n \simeq \frac{1}{|C_i|}\int_{C_i} X(\mathbf{x}, t^n)d\mathbf{x}. \tag{3.7}$$

Then, the approximation of the prediction step (3.1) can be summarized as follows

$$H_i^{n+1/2} = H_i^n - \sum_{j\in\mathcal{K}_i} \sigma_{ij}\mathcal{F}_H(X_i^{*,n}, X_j^{*,n}) - \sigma_i\mathcal{F}_H(X_i^n, X_{e,i}^n), \tag{3.8}$$

$$(H\mathbf{u})_i^{n+1/2} = (H\mathbf{u})_i^n - \sum_{j\in\mathcal{K}_i} \sigma_{ij}\mathcal{F}_{H\mathbf{u}}(X_i^{*,n}, X_j^{*,n}) + \sum_{j\in\mathcal{K}_i} \sigma_{ij}\mathcal{S}(X_i^n, X_i^{*,n}) - \sigma_i\mathcal{F}_{H\mathbf{u}}(X_i^n, X_{e,i}^n), \tag{3.9}$$

where the quantity σ_{ij} depends on $|C_i|$, on Δt^n and on the length of the cell edges. Similarly, $\sigma_i \doteq \sigma_{ii}$ is computed for the boundary cells of the domain and $X_{e,i}^n$ is a fictive state associated to a cell C_i at the boundary of the domain (see [20]). The fluxes $\mathcal{F}_H$ (resp. $\mathcal{F}_{H\mathbf{u}}$) are the numerical fluxes corresponding to H (resp. $H\mathbf{u}$). We do not give details on these fluxes. The hydrostatic reconstruction (HR) technique ensures the well-balancing of the scheme (see [6]). Hence the term $\mathcal{S}$ in Eq. (3.9) is an adapted discretization of the topography source term S in Eq. (3.1). Notice also that in Eqs. (3.8),(3.9), the superscript * means that the considered variable is reconstructued according to the HR technique [6]. For the numerical results presented in this paper, the numerical fluxes are computed by a kinetic solver coupled with a hydrostatic reconstruction technique (see [7]) but other choices are possible. In Eq. (3.9), the boundary conditions (2.8)-(2.10) are treated as a Riemann problem at the interface (see [20, 3] for more details about the treatment of the boundary conditions for the shallow water system).

For the third component of Eq. (3.9), we consider

$$(Hw)_i^{n+1/2} = (Hw)_i^n - \sum_{j\in\mathcal{K}_i} \sigma_{ij}\mathcal{F}_H(X_i^n, X_j^n)\left(w_i^n\mathbf{1}_{\mathcal{F}_H(X_i^n,X_j^n)\geq 0} + w_j^n\mathbf{1}_{\mathcal{F}_H(X_i^n,X_j^n)\leq 0}\right)$$
$$- \sigma_i\mathcal{F}_H(X_i^n, X_{e,i}^n)\left(w_i^n\mathbf{1}_{\mathcal{F}_H(X_i^n,X_{e,i}^n)\geq 0} + w_{e,i}^n\mathbf{1}_{\mathcal{F}_H(X_i^n,X_{e,i}^n)\leq 0}\right). \tag{3.10}$$

Classically, Δt^n satisfies a CFL condition ensuring the stability of the scheme (mainly domain invariant). Notice that the resolution of the correction step (3.2)-(3.3) is implicit and does not add any constraint over Δt^n.

3.4. **The mixed problem**

Considering now that $X^{n+1/2}$ is given by Eq. (3.1), we study the mixed problem corresponding to the correction step, that is to say the system (3.2)-(3.3), and we give a variational formulation of the problem together with an appropriate treatment of the boundary conditions at the continuous level in order to be compatible with the hyperbolic part. This will make it possible to construct the finite element scheme for this problem. To do so, we consider the domain Ω depicted over Fig. 2.1 with the boundary conditions (2.8),(2.10). The correction step consists in computing the shallow water pressure p in order to satisfy the shallow water divergence free condition (3.3). Notice that the water depth H computed by Eq. (3.1) is not modified by the correction step which reads

$$H^{n+1} = H^{n+1/2}, \tag{3.11}$$

$$(Hu)^{n+1} + \Delta t^n \left(H^{n+1} \frac{\partial p^{n+1}}{\partial x} + p^{n+1} \frac{\partial \zeta^{n+1}}{\partial x} \right) = (Hu)^{n+1/2}, \tag{3.12}$$

$$(Hv)^{n+1} + \Delta t^n \left(H^{n+1} \frac{\partial p^{n+1}}{\partial y} + p^{n+1} \frac{\partial \zeta^{n+1}}{\partial y} \right) = (Hv)^{n+1/2}, \tag{3.13}$$

$$(Hw)^{n+1} - \gamma \Delta t^n \, p^{n+1} = (Hw)^{n+1/2}, \tag{3.14}$$

completed with the divergence free condition (3.3) and the boundary conditions discretized from (2.8), (2.10). From now on, we drop the superscript $^{n+1}$ and note Δt for Δt^n, thus the system (3.12)-(3.14) and (3.3) is written

$$H\mathbf{u} + \Delta t \nabla_{sw}^{\gamma} p = H\mathbf{u}^{n+1/2}, \tag{3.15}$$

$$\mathrm{div}_{sw}^{\gamma}(\mathbf{u}) = 0, \tag{3.16}$$

where H denotes the water depth $H^{n+1} = H^{n+1/2}$. This mixed problem in velocity/pressure leads to solving the pressure equation (3.4), and then to update the velocity with the equation (3.15). Equations (3.15)-(3.16) are the "grad-div" formulation of the problem. The boundary conditions for the system (3.15)-(3.16) need to be detailed since they have to be consistent with the prediction part. This is done in the following paragraph.

3.4.1. *Compatible boundary conditions*

In geophysical models such as the shallow water model, it is usual to impose an inflow condition on the inlet Γ_{in}, namely $H\mathbf{u}$, and the water depth at the outflow or a free outflow, as defined by (2.8) and (2.9). For the hyperbolic step, this choice depends on the Froude number $Fr = \frac{|\mathbf{u}|}{\sqrt{gH}}$ which characterizes the flow (fluvial or torrential). In this part, we apply compatible boundary conditions on the mixed system depending on the regime chosen for the corresponding Saint-Venant problem at the prediction step. The mixed formulation will allow us to impose boundary conditions on the velocity or the pressure.

Inflow /outflow. Let us take the two-dimensional inflow $\mathbf{Q}_e = ((Hu)_e^{n+1/2}, (Hv)_e^{n+1/2})^T$ which is imposed at the hyperbolic part; the vertical velocity w_e will be treated independently, see Eq. (3.10). Many strategies can be applied to satisfy compatible boundary conditions. As can be seen in the equations (3.12)-(3.13), a natural choice is to keep $\mathbf{Q}_e$ the same as in the hyperbolic part, then we will impose a condition on the inlet velocity $\mathbf{u} \cdot \mathbf{n} = (u_e, v_e, w_e)^T \cdot \mathbf{n}$ on Γ_{in}.

Considering the pressure equation (3.4) and following the procedure detailed in [2], we can deduce that this corresponds to apply a shallow water version of a Neumann boundary condition for the

pressure i.e.

$$\nabla_{sw}^{\gamma} p \cdot \mathbf{n} = 0 \text{ on } \Gamma_{in}. \tag{3.17}$$

In contrast, for the outflow, we impose the water depth in the hyperbolic step and recommend a Dirichlet boundary condition for the pressure in order to let the discharge free at the outlet, namely $p|_{\Gamma_{out}} = p^a = cst$.

3.4.2. *Slip boundary conditions*

For the wall of the channel represented by Γ_s in Fig. 2.1, we assume a slip condition for the hyperbolic part $\mathbf{u}^{n+1/2} \cdot \mathbf{n}|_{\Gamma_s} = 0$ with a Neumann boundary condition for H (see [20]) and we maintain this condition in the dispersive part, namely $\mathbf{u} \cdot \mathbf{n}|_{\Gamma_s} = 0$. Still from the pressure equation (3.4) and in the same spirit as in [2], we deduce that this leads to having $\nabla_{sw}^{\gamma} p \cdot \mathbf{n}|_{\Gamma_s} = 0$. Since $\frac{\partial H}{\partial x}|_{\Gamma_s} = 0$, it gives a Neumann-type boundary condition for the pressure $\frac{\partial p}{\partial \mathbf{n}} = 0$ on Γ_s.

3.4.3. *The variational formulation*

First of all, we assume $\nabla\zeta \in (L^{\infty}(\Omega))^2$, $p_0 \in H^{-1/2}(\Gamma)$ and we assume $H \in L^{\infty}(\Omega)$ is bounded below and above

$$\alpha_1 < H < \alpha_2, \quad \alpha_1, \alpha_2 > 0. \tag{3.18}$$

In this section we give the variational formulation of the mixed problem (3.15)-(3.16) completed with appropriate boundary conditions

$$\mathbf{u} \cdot \mathbf{n} = \mathbf{u}^{n+1/2} \cdot \mathbf{n} \ \text{ on } \Gamma_{in}, \qquad \mathbf{u} \cdot \mathbf{n} = 0 \quad \text{on } \Gamma_s, \tag{3.19}$$

$$p = p_0 \quad \text{on } \Gamma_{out}. \tag{3.20}$$

In (3.20), to give a general formulation, we have considered a non-homogeneous Dirichlet boundary condition for the pressure.

Now we distinguish two variational formulations using the shallow water divergence or gradient operator and we explain how to choose the most judicious one in practice. Notice that we switch from one formulation to the other using the relation (2.35).

Formulation using the shallow water divergence operator. In this section, we will propose a strong treatment of the boundary condition for the velocity, we introduce the spaces

$$\mathbf{V} = \{\mathbf{v} \in L^2(\Omega)^3, \ \mathrm{div}_{sw}^{\gamma}(\mathbf{u}) \in L^2(\Omega)\}, \tag{3.21}$$

$$\mathbf{W} = \{\mathbf{w} \in \mathbf{V}, \ \mathbf{w} \cdot \mathbf{n} = 0 \text{ on } \Gamma_{in} \cup \Gamma_s\}. \tag{3.22}$$

The Hilbert space $\mathbf{W}$ is equipped with inner product $(.,.)_{\mathbf{W}}$ and induced norm $||.||_{\mathbf{W}} = ||.||_{(\mathbf{L^2(\Omega)})^3} + ||\mathrm{div}_{sw}^{\gamma}(.)||_{\mathbf{L^2(\Omega)}}$. For this variational formulation, we assume a homogeneous boundary condition for the velocity, namely, in (3.19) we take $\mathbf{u} \cdot \mathbf{n} = 0$ on Γ_{in}.
Then the problem (3.15)-(3.16) reads:
Find $\mathbf{u} \in \mathbf{W}$, $p \in L^2(\Omega)$ such that, $\forall\, \mathbf{v} \in \mathbf{W}$,

$$\int_{\Omega} H\mathbf{u} \cdot \mathbf{v} \, d\mathbf{x} - \Delta t \int_{\Omega} \mathrm{div}_{sw}^{\gamma}(\mathbf{v})\, p \, d\mathbf{x} = \int_{\Omega} H\mathbf{u}^{n+1/2} \cdot \mathbf{v} \, d\mathbf{x} - < H\mathbf{v} \cdot \mathbf{n}, p_0 >_{\Gamma_{out}}, \tag{3.23}$$

$$\int_{\Omega} \mathrm{div}_{sw}^{\gamma}(\mathbf{u}) q \, d\mathbf{x} = 0, \quad \forall q \in L^2(\Omega), \tag{3.24}$$

where we assume $p_0 \in H^{-1/2}(\Gamma_{out})$ and $< \cdot, \cdot >_{\Gamma_{out}}$ represents the duality between $H^{-1/2}(\Gamma_{out})$ and $H^{1/2}(\Gamma_{out})$ and $\mathbf{u}^{n+1/2} \in \mathbf{W}$. We introduce the bilinear forms

$$a(\mathbf{u}, \mathbf{v}) = \int_\Omega H\mathbf{u} \cdot \mathbf{v} d\mathbf{x}, \quad \forall \mathbf{u}, \mathbf{v} \in \mathbf{V}, \tag{3.25}$$

$$b_\gamma(\mathbf{v}, q) = -\int_\Omega \mathrm{div}_{sw}^\gamma(\mathbf{v})\, q\, d\mathbf{x}, \quad \forall \mathbf{v} \in \mathbf{W}\ , \forall q \in L^2(\Omega). \tag{3.26}$$

The problem reads:
Find $\mathbf{u} \in \mathbf{W}$, $p \in L^2(\Omega)$ such that

$$a(\mathbf{u}, \mathbf{v}) - \Delta t\, b_\gamma(\mathbf{v}, p) = a(H\mathbf{u}^{n+1/2}, \mathbf{v}) - < H\mathbf{v} \cdot \mathbf{n}\ , p_0 >_{\Gamma_{out}}, \quad \forall \mathbf{v} \in \mathbf{W}, \tag{3.27}$$

$$b_\gamma(\mathbf{u}, q) = 0, \quad \forall q \in L^2(\Omega). \tag{3.28}$$

To impose a non-homogeneous boundary condition on Γ_s for the velocity $\mathbf{u}$, we choose $\mathbf{u} - \bar{\mathbf{u}}_0 \in \mathbf{W}$ where $\bar{\mathbf{u}}_0$ is defined on $\bar{\Omega}$ such that $\bar{\mathbf{u}}_0|_{\Gamma_s} = \mathbf{u}^{n+1/2}|_{\Gamma_s}$.
In practice, this formulation requires to choose basis functions satisfying the slip condition in (3.22). Therefore, if we want to have a domain with a specific boundary, we will prefer the formulation using the shallow water gradient operator, which is described in the following.

Formulation using the shallow water gradient operator. We define the spaces

$$Q = \{q \in L^2(\Omega), \nabla_{sw}^\gamma q \in L^2(\Omega)^3\}, \quad Q_0 = \{q \in Q\ ,\ q|_{\Gamma_{out}} = 0\}.$$

Using the duality relation (2.35), we have

$$\int_\Omega \nabla_{sw}^\gamma(q) \cdot \mathbf{u}\, d\mathbf{x} - \int_\Gamma qH\mathbf{u} \cdot \mathbf{n}\, ds = 0, \quad \forall q \in Q,$$

then writing

$$\int_\Gamma qH\mathbf{u} \cdot \mathbf{n}\, ds = \int_{\Gamma_{in}} qH\mathbf{u} \cdot \mathbf{n}\, ds + \int_{\Gamma_s} qH\mathbf{u} \cdot \mathbf{n}\, ds + \int_{\Gamma_{out}} qH\mathbf{u} \cdot \mathbf{n}\, ds, \tag{3.29}$$

and, using the boundary conditions (3.19)-(3.20), we have

$$\int_\Gamma qH\mathbf{u} \cdot \mathbf{n}\, ds = \int_{\Gamma_{in}} qH\mathbf{u}^{n+1/2} \cdot \mathbf{n}\, ds,$$

where the slip boundary condition is imposed in the following weak form $\int_{\Gamma_s} qH\mathbf{u} \cdot \mathbf{n} = 0$, $\forall q \in Q$. We apply the procedure proposed for the Navier-Stokes equations in [41] and we assume there exists $\bar{p}_0 \in Q$ a given pressure such that $p_0 = \bar{p}_0|_{\Gamma_{out}} \in H^{1/2}(\Gamma_{out})$. Therefore, the problem (3.15)-(3.16) completed with (3.19)-(3.20) reads:
Find $\tilde{p} = p - \bar{p}_0 \in Q_0$, $p \in Q$, $\mathbf{u} \in (L^2(\Omega))^3$ such that,

$$\int_\Omega (H\mathbf{u} + \Delta t \nabla_{sw}^\gamma \tilde{p}) \cdot \mathbf{v}\, d\mathbf{x} = \int_\Omega H\mathbf{u}^{n+1/2} \cdot \mathbf{v}\, d\mathbf{x}, \quad \forall \mathbf{v} \in (L^2(\Omega))^3,$$

$$\int_\Omega \nabla_{sw}^\gamma(q).\mathbf{u}\, d\mathbf{x} = \int_{\Gamma_{in}} qH\mathbf{u}^{n+1/2} \cdot \mathbf{n}\, ds, \quad \forall q \in Q_0.$$

Finally, we consider the following problem:
Find $\mathbf{u} \in (L^2(\Omega))^3$, $p \in Q$ such that, $\forall \mathbf{v} \in (L^2(\Omega))^3$,

$$\int_\Omega (H\mathbf{u} + \Delta t \nabla_{sw}^\gamma p) \cdot \mathbf{v}\, d\mathbf{x} = \int_\Omega H\mathbf{u}^{n+1/2} \cdot \mathbf{v}\, d\mathbf{x} - \Delta t \int_\Omega \nabla_{sw}^\gamma \bar{p}_0 \cdot \mathbf{v}\, d\mathbf{x}, \tag{3.30}$$

$$\int_\Omega \nabla_{sw}^\gamma(q).\mathbf{u}\, d\mathbf{x} = \int_{\Gamma_{in}} qH\mathbf{u}^{n+1/2} \cdot \mathbf{n}\, ds, \quad \forall q \in Q_0.$$

As already mentioned, notice that we can use this formulation with the shallow water gradient operator instead of the formulation (3.23)-(3.24) with the divergence operator in order to avoid choosing basis functions satisfying the slip boundary condition.

The pressure equation. Following the procedure of the one-dimensional problem in [2], we set $\mathbf{v} = \frac{\nabla_{sw}^{\gamma}(q)}{H}$ in (3.30) and take homogeneous boundary conditions for the pressure on Γ. It leads to a variational formulation of the problem in the form

$$(\Delta_{sw}^{\gamma} p, q) = \frac{1}{\Delta t^n}\left(\mathrm{div}_{sw}^{\gamma}(\mathbf{u}^{n+1/2}), q\right), \quad \forall q \in Q_{0,sw}, \tag{3.31}$$

where

$$Q_{sw} = \{q \in Q, |\mathrm{div}_{sw}^{\gamma}\left(\frac{\nabla_{sw}^{\gamma} q}{H}\right) \in L^2(\Omega)\}, \quad Q_{0,sw} = \{q \in Q_{sw}, \ \ q|_{\Gamma} = 0\},$$

and the operator Δ_{sw}^{γ} is the Laplacian operator defined by (3.4).

3.4.4. *The inf-sup condition*

We want to establish the inf-sup condition at the continuous level to ensure the problem is well-posed. The so-called inf-sup condition was introduced by Ladyzhenskaya, Babuska and Brezzi in [8, 19, 42] to ensure the well-posedness of mixed problems for incompressible flows and it has been studied for the finite element method for instance in [30]. We consider the variational problem with Dirichlet boundary conditions for the pressure (3.20). The problem (3.27)-(3.28) is under the form:
Find $\mathbf{u} \in \mathbf{W}$, $p \in L^2(\Omega)$ such that

$$\begin{aligned} a(\mathbf{u}, \mathbf{v}) - \Delta t \; b_{\gamma}(\mathbf{v}, p) &= a(\mathbf{f}, \mathbf{v}) - < H\mathbf{v}\cdot\mathbf{n}\,, p_0 >_{\Gamma_{out}}, \quad \forall \mathbf{v} \in \mathbf{W}, \\ b_{\gamma}(\mathbf{u}, q) &= 0, \quad \forall q \in L^2(\Omega), \end{aligned}$$

where $\mathbf{f} \in \mathbf{W}$ is a given vector. For all $\mathbf{v} \in \mathbf{W}_0 = \{\mathbf{v} \in \mathbf{W}\,, \mathrm{div}_{sw}^{\gamma}(\mathbf{v}) = 0\}$, the problem becomes:
Find $\mathbf{u} \in \mathbf{W}_0$ such that

$$a(\mathbf{u}, \mathbf{v}) = a(\mathbf{f}, \mathbf{v}) - < H\mathbf{v}\cdot\mathbf{n}\,, p_0 >_{\Gamma_{out}}, \quad \forall \mathbf{v} \in \mathbf{W}_0.$$

Under the assumption (3.18), it is obvious that the bilinear form a is coercive, i.e. for all $\mathbf{v} \in \mathbf{W}_0$

$$a(\mathbf{v}, \mathbf{v}) \geq \alpha_1 ||\mathbf{v}||^2_{L^2(\Omega)}, \ \ \alpha_1 > 0.$$

In addition, b_{γ} is bilinear. With the assumption (3.18), and $q \in L^2(\Omega)$ given, if we choose

$$\mathbf{v} = (0, 0, q)^T, \tag{3.32}$$

then

$$\frac{b_{\gamma}(\mathbf{v}, q)}{||q||_{L^2(\Omega)}} = \gamma ||q||_{L^2(\Omega)}. \tag{3.33}$$

Using now classical results (see e.g. [19]), this implies the existence and uniqueness of the solution of (3.23)-(3.24). For the formulation with the operator ∇_{sw}^{γ}, we can use a similar argument and take $\mathbf{v} = \nabla_{sw}^{\gamma}(q)$.

4. **Finite element approximations for the mixed problem**

In this part, we apply a finite element approximation for the correction part (3.15)-(3.16), which is suitable to solve the elliptic problem for the pressure. We need two discrete spaces, one for the velocity and one for the approximation of the pressure.

Sketch of a possible choice. In practice, the choice of the formulation should be done in function of the boundary conditions. We can summarize the idea by the following

- Unless for very specific cases, it is usual to impose a homogeneous boundary condition for the pressure since we don't know the value of the pressure in real geophysical situations, then the formulations using the gradient or the divergence shallow water operator are both appropriate.

- The choice will also concern the boundary conditions for the velocity, and more precisely for $\mathbf{u} \cdot \mathbf{n}$. Using the shallow water divergence operator, it is necessary to build a discrete space with basis functions satisfying slip boundary conditions. In addition, if a discharge is imposed, a lifting of the boundary condition should be applied.

- Besides, we look for a couple of spaces such that the inf-sup condition is satisfied.

In the numerical method presented below, we use the divergence shallow water formulation (see paragraph 3.4.3), with two examples of implementation such that the inf-sup condition is satisfied. Indeed for this formulation, it is straightforward to find spaces such that this condition is verified. Using the same argument as for the continuous problem, we choose spaces such that the conditions (3.32) and (3.33) are verified at the discrete level.

The two proposed implementations are, first the $\mathrm{P}_1/\mathrm{P}_1$ spaces and then the P_1-iso$\mathrm{P}_2/\mathrm{P}_1$ spaces. As usual, P_k denotes the space of polynomials of two variables of degree $\leq k$, and $\mathrm{P}_j/\mathrm{P}_i$ denotes the pair of approximation spaces where P_j is related to the velocity and P_i is related to the pressure. For the pair $\mathrm{P}_1/\mathrm{P}_1$, the velocity w is approximated in the same approximation space as the pressure, and for the pair P_1-iso$\mathrm{P}_2/\mathrm{P}_1$, the approximation space of w contains the approximation space of the pressure (see paragraph 4.2). For both, we give the discrete formulation and we provide a comparison of the numerical results (see Section 6.1) in order to choose the most accurate solution. Since, in this paper, we intend to present simple cases, we will treat numerical applications on domains (rectangles) where the condition $\mathbf{u} \cdot \mathbf{n} = 0$ reduces to $u = 0$ or $v = 0$ (otherwise see [41]).

It is possible to define other function spaces satisfying the inf-sup condition but we have singled out strategies where reduced stencils arise especially due to the difficulties coming from the numerical treatment of the boundary conditions.

4.1. The $\mathbf{P}_1/\mathbf{P}_1$ approximation

For this first implementation, we choose a $\mathrm{P}_1/\mathrm{P}_1$ finite element approximation (see [52, 30]) on the primal mesh $\mathcal{T}$ introduced in paragraph 3.2, on which we approximate the variables at the nodes of the triangles (see Fig. 3.1). We give the discrete problem with the following boundary conditions

$$p = 0, \text{ on } \Gamma_{out}, \tag{4.1}$$

$$\mathbf{u} \cdot \mathbf{n} = 0, \text{ on } \Gamma_s \cup \Gamma_{in}. \tag{4.2}$$

Let us introduce the discrete spaces of approximation:

$$V_h = \{v_h \in C_0(\Omega_h), v_h|_T \in \mathrm{P}_1, \ \forall\, T \in \mathcal{T}\ \},$$
$$Q_h = \{q_h \in C_0(\Omega_h), q_h|_T \in \mathrm{P}_1, \ \forall\, T \in \mathcal{T}\},$$

with the dimensions $\dim(Q_h) = M$, $\dim(V_h) = N$. We denote $\mathbf{V}_h = (V_h)^3$. Because of the $\mathrm{P}_1/\mathrm{P}_1$ approximation, V_h and Q_h coincide but we keep two distinct notations in order to be consistent with the notations that will be used in the P_1-iso$\mathrm{P}_2/\mathrm{P}_1$ context, see paragraph 4.2.

We use a strong treatment of the boundary condition for the velocity. Therefore, we take

$$\mathbf{u}_h \in \mathbf{W}_h = \{\mathbf{v}_h \in \mathbf{V}_h, \ \ \mathbf{v}_h \cdot \mathbf{n}|_{\Gamma_s} = 0\},$$

and $p_h \in Q_h$ respectively the piecewise linear approximations of $\mathbf{u}$ and p on the triangles of $\mathcal{T}$. Notice that the normal components are evaluated by mean for each boundary node in order to impose the

slip boundary condition $\mathbf{v}_h \cdot \mathbf{n}|_{\Gamma_s} = 0$. In addition, we assume $H_h \in V_h$, $\zeta_h \in V_h$, so we introduce

$$p_h(\mathbf{x}) = \sum_{j \in \mathcal{J}_M} p_j \varphi_j(\mathbf{x}), \quad H_h(\mathbf{x}) = \sum_{i \in \mathcal{I}_N} H_i \varphi_i(\mathbf{x}), \tag{4.3}$$

$$(H\mathbf{u})_h(\mathbf{x}) = \sum_{i \in \mathcal{I}_N} (H\mathbf{u})_i \varphi_i(\mathbf{x}), \qquad \zeta_h(\mathbf{x}) = \sum_{i \in \mathcal{I}_N} \zeta_i \varphi_i, \tag{4.4}$$

where $\mathcal{I}_N$ (resp. $\mathcal{J}_M$) is the set of indices of the space V_h (resp. Q_h) and $\{\varphi_j\}_{j \in \mathcal{J}_M}$ (resp. $\{\varphi_i\}_{i \in \mathcal{I}_N}$) are the basis functions of Q_h (resp. V_h) and

$$\mathbf{u}_h(\mathbf{x}) = \sum_{i \in \mathcal{I}_N} \mathbf{u}_i \varphi_i(\mathbf{x}), \tag{4.5}$$

$$\mathbf{u}_i = \begin{pmatrix} u_i \\ v_i \\ w_i \end{pmatrix} = \frac{1}{H_i} \begin{pmatrix} (Hu)_i \\ (Hv)_i \\ (Hw)_i \end{pmatrix}. \tag{4.6}$$

Remark 4.1. Notice that the differences between the two sets of indices $\mathcal{I}_N$ and $\mathcal{J}_M$ are due to the type of boundary conditions prescribed at the nodes.

We use the definitions (4.6) in accordance with the finite volume approximation (3.8)-(3.9) (see Remark 3.2) and we will use mass lumping in the integrals to be consistent with these definitions.

The discrete formulation of problem (3.23)-(3.24) reads:
Find $\mathbf{u}_h \in \mathbf{W_h}$, $p_h \in Q_h$ such that

$$\int_\Omega H_h \mathbf{u}_h \cdot \mathbf{v}_h \, d\mathbf{x} + \Delta t \int_\Omega \mathrm{div}_{sw}^{\gamma}(\mathbf{v}_h) p_h \, d\mathbf{x} = \int_\Omega H_h \mathbf{u}_h^{n+1/2} \cdot \mathbf{v}_h \, d\mathbf{x}, \quad \forall \mathbf{v}_h \in \mathbf{W_h}, \tag{4.7}$$

$$\int_\Omega \mathrm{div}_{sw}^{\gamma}(\mathbf{u}_h) q_h \, d\mathbf{x} = 0 \quad \forall q_h \in Q_h. \tag{4.8}$$

In order to describe the method, we introduce the following notations

- $S_h = \{s_i = (x_i, y_i) \in \mathcal{T}\}$: the vertices of the triangular mesh (see (3.6)),
- $K_{h,i} = \{T \in \mathcal{T} | s_i \in T\}$: the triangles connected to a vertex s_i.

Using the definitions (4.3)-(4.6), Eqs. (4.7)-(4.8) become

$$\begin{aligned} &\sum_{i \in \mathcal{I}_N} \left(\int_\Omega H_i \mathbf{u}_i \varphi_i(\mathbf{x}) \cdot \mathbf{v}_h(\mathbf{x}) \, d\mathbf{x} \right) - \sum_{j \in \mathcal{J}_M} \Delta t \left(\int_\Omega \mathrm{div}_{sw}^{\gamma}(\mathbf{v}_h(\mathbf{x})) \varphi_j(\mathbf{x}) \, d\mathbf{x} \right) p_j \\ &= \sum_{i \in \mathcal{I}_N} \left(\int_\Omega H_i \mathbf{u}_i^{n+1/2} \varphi_i(\mathbf{x}) \cdot \mathbf{v}_h(\mathbf{x}) \, d\mathbf{x} \right), \quad \forall \mathbf{v}_h \in \mathbf{W_h}, \end{aligned} \tag{4.9}$$

completed with the divergence free condition

$$\sum_{i \in \mathcal{I}_N} \left(\int_\Omega \mathrm{div}_{sw}^{\gamma}(\varphi_i) \, q_h \, \mathbf{u}_i \, d\mathbf{x} \right) = 0, \quad \forall q_h \in Q_h. \tag{4.10}$$

We introduce the pressure vector $P = (p_j)_{1 \le j \le M}$ and the velocity vector $U = (U_1, U_2, U_3)^T$, with $U_1 = (u_i)_{1 \le i \le N}$, $U_2 = (v_i)_{1 \le i \le N}$, and $U_3 = (w_i)_{1 \le i \le N}$. Then the problem (4.9)-(4.10) can be written as

$$A_H U + \Delta t B_\gamma^T P = A_H U^{n+1/2}, \tag{4.11}$$

$$B_\gamma U = 0, \tag{4.12}$$

with the classical notations (see [52]) for the mass matrix A_H, and the divergence operator matrix B_γ. The matrix A_H depends on the water depth H and is composed of the three diagonal matrices M_H

$$A_H = \begin{pmatrix} M_H & 0 & 0 \\ 0 & M_H & 0 \\ 0 & 0 & M_H \end{pmatrix},$$

with $M_{H\,ji}$ the approximation of $\sum_{T\in K_{h,i}} \int_T H_i\varphi_i\varphi_j d\mathbf{x}$. More precisely, using mass lumping we obtain

$$M_{Hji} = \sum_{T\in K_{h,i}} \frac{|T|}{3} H_i \delta_{ij}. \tag{4.13}$$

We have denoted by B_γ the shallow water divergence operator defined by (4.10) with $B_\gamma = (B_{\gamma,1}, B_{\gamma,2}, B_{\gamma,3})$ and using the definition of $\mathrm{div}_{sw}^{\gamma}$ in (2.33), we obtain

$$B_{\gamma,1\,ji} = -\sum_{T\in K_{h,i}} \int_T \frac{\partial H_h\varphi_i}{\partial x}\varphi_j d\mathbf{x} + \sum_{T\in K_{h,i}} \int_T \varphi_i\varphi_j \frac{\partial \zeta_h}{\partial x} d\mathbf{x},$$

$$B_{\gamma,2\,ji} = -\sum_{T\in K_{h,i}} \int_T \frac{\partial H_h\varphi_i}{\partial y}\varphi_j d\mathbf{x} + \sum_{T\in K_{h,i}} \int_T \varphi_i\varphi_j \frac{\partial \zeta_h}{\partial y} d\mathbf{x}, \quad B_{\gamma,3\,ji} = -\gamma \sum_{T\in K_{h,i}} \int_T \varphi_i\varphi_j d\mathbf{x}.$$

Finally, the linear system (4.11)-(4.12) reads

$$\begin{pmatrix} \frac{1}{\Delta t}M_H & 0 & 0 & B_{\gamma,1} \\ 0 & \frac{1}{\Delta t}M_H & 0 & B_{\gamma,2} \\ 0 & 0 & \frac{1}{\Delta t}M_H & B_{\gamma,3} \\ B_{\gamma,1}^T & B_{\gamma,2}^T & B_{\gamma,3}^T & 0 \end{pmatrix} \begin{pmatrix} U_1 \\ U_2 \\ U_3 \\ P \end{pmatrix} = \frac{1}{\Delta t} \begin{pmatrix} M_H & 0 & 0 \\ 0 & M_H & 0 \\ 0 & 0 & M_H \\ 0 & 0 & 0 \end{pmatrix} \begin{pmatrix} U_1^{n+1/2} \\ U_2^{n+1/2} \\ U_3^{n+1/2} \end{pmatrix}.$$

By analogy with the continuous problem, applying the matrix B_γ to the equation (4.11), we obtain the discrete elliptic equation for the pressure

$$B_\gamma A_H^{-1} B_\gamma^T P = B_\gamma U^{n+1/2}, \tag{4.14}$$

which is the discretization of the pressure equation (3.31). We now give some numerical approximations of the integrals we use for each matrix. The matrix B_γ is computed with the following formulas

$$\begin{aligned} B_{\gamma,1\,ji} = &-\sum_{T\in K_{h,i}} \frac{\partial H_h}{\partial x}\Big|_T \int_T \varphi_i\varphi_j \, d\mathbf{x} - \sum_{T\in K_{h,i}} \frac{\partial \varphi_i}{\partial x}\Big|_T \int_T H_h\varphi_j \, d\mathbf{x} \\ &+ \sum_{T\in K_{h,i}} \frac{\partial \zeta_h}{\partial x}\Big|_T \int_T \varphi_i\varphi_j \, d\mathbf{x}, \\ B_{\gamma,2\,ji} = &-\sum_{T\in K_{h,i}} \frac{\partial H_h}{\partial y}\Big|_T \int_T \varphi_i\varphi_j \, d\mathbf{x} - \sum_{T\in K_{h,i}} \frac{\partial \varphi_i}{\partial y}\Big|_T \int_T H_h\varphi_j \, d\mathbf{x} \\ &+ \sum_{T\in K_{h,i}} \frac{\partial \zeta_h}{\partial y}\Big|_T \int_T \varphi_i\varphi_j \, d\mathbf{x}, \\ B_{\gamma,3\,ji} = &-\gamma \sum_{T\in K_{h,i}} \frac{|T|}{3}\delta_{ij}. \end{aligned}$$

In the first terms of $B_{\gamma,1\,ji}$ and $B_{\gamma,2\,ji}$, we use definition (4.3) of H_h with mass lumping, and we obtain

$$\int_T H_h\varphi_j \, d\mathbf{x} = \sum_k \int_T H_k\varphi_k\varphi_j \, d\mathbf{x} = \int_T H_i\varphi_j \, d\mathbf{x} = \frac{|T|}{3} H_i. \tag{4.15}$$

The projection of the shallow water divergence on a vertex of the mesh is defined by $\forall \mathbf{u}_h \in \mathbf{W}_h, \forall j \in \mathcal{J}_M$

$$\mathrm{div}_{sw}^{\gamma}(\mathbf{u}_h)|_j = \frac{3}{\mathrm{supp}(\varphi_j)} \sum_{i \in \mathcal{I}_N} \int_\Omega \mathrm{div}_{sw}^{\gamma}(\varphi_{\mathbf{i}}(\mathbf{x}))\varphi_j(\mathbf{x})\, d\mathbf{x}\, \mathbf{u}_i, \tag{4.16}$$

where $\mathrm{supp}(\varphi_j)$ is the area of the support of the function φ_j and is computed by $\mathrm{supp}(\varphi_j) = \sum_{T \in K_{h,j}} |T|)$.

4.2. A P_1-isoP$_2$/P$_1$ approximation

In this part, we propose another approximation by finite elements, using the spaces P_1-isoP$_2$/P$_1$ (see [52]) in which we define a coarse triangular mesh $\mathcal{T}_{2h}$ and a fine mesh $\mathcal{T}_h$. The fine mesh corresponds to the primal mesh introduced for the finite volume method 3.3. Unlike the previous approach, the velocity and the pressure are defined in two different spaces. This allows us to approximate the pressure on a coarser mesh than the velocity. Let us introduce the discrete spaces of approximation

$$V_h = \{v_h \in C_0(\Omega_h),\ \mathbf{v}_h|_\tau \in \mathrm{P}_1,\ \forall\, \tau \in \mathcal{T}_h\}, \quad Q_h = \{q_h \in C_0(\Omega_h),\ q_h|_T \in \mathrm{P}_1,\ \forall\, T \in \mathcal{T}_{2h}\},$$

with the dimensions $\dim(V_h) = N$ and $\dim(Q_h) = M$. In addition, we assume $H_h \in V_h$. In practice, the triangulation $\mathcal{T}_h$ is obtained by subdividing each triangle $T \in \mathcal{T}_{2h}$ into four triangles τ by joining the middle of the edges, as shown in Fig. 4.1.

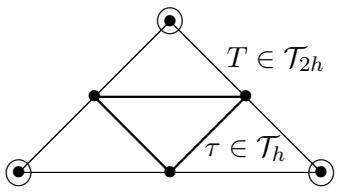

Figure 4.1. Representation of the triangulation. The velocity is evaluated on the black nodes, while the pressure is evaluated on the circles.

In these approximation spaces, the velocity is evaluated with the same degrees of freedom as for the P_2 space on the coarse mesh.
In order to describe the method, we introduce the following notations

- $S_h = \{s_i = (x_i, y_i) \in \mathcal{T}_h\}$: the vertices of the fine mesh,
- $S_{2h} = \{s_j = (x_j, y_j) \in \mathcal{T}_{2h}\}$: the vertices of the coarse mesh,
- $K_{h,i} = \{\tau \in \mathcal{T}_h | s_i \in \tau\}$: the triangles of the fine mesh connected to node s_i,
- $K_{2h,j} = \{T \in \mathcal{T}_{2h} | s_j \in T\}$: the triangles of the coarse mesh connected to node s_j.

We take $\mathbf{u}_h \in \mathbf{W}_h$ and $p_h \in Q_h$, with $\mathbf{W}_h = \{\mathbf{v}_h \in \mathbf{V}_h,\ \ \mathbf{v}_h \cdot \mathbf{n}|_{\Gamma_s} = 0\}$,

$$p_h(\mathbf{x}) = \sum_{j \in \mathcal{J}_M} p_i \phi_j(\mathbf{x}), \quad H_h = \sum_{i \in \mathcal{I}_N} H_i \varphi_i(\mathbf{x}), \quad (H\mathbf{u})_h = \sum_{i \in \mathcal{I}_N} (H\mathbf{u})_i \varphi_i(\mathbf{x}),$$

where ϕ_j (resp. φ_i) are the basis functions of Q_h (resp. V_h) and

$$\mathbf{u}_h(\mathbf{x}) = \sum_{i \in \mathcal{I}_N} \mathbf{u}_i \varphi_i(\mathbf{x}),$$

with $\mathbf{u}_i$ defined as in (4.5). Then the matrix B is computed with the following formulas

$$\begin{aligned}
B_{\gamma,1\,ji} &= -\sum_{T\in K_{2h,i}} \frac{\partial \phi_j}{\partial x}\Big|_T \sum_{\tau\in T}\int_\tau H_h\varphi_i\, d\mathbf{x} - \sum_{T\in K_{2h,i}} \frac{\partial H_h}{\partial x}\Big|_T \sum_{\tau\in T}\int_\tau \phi_j\varphi_i\, d\mathbf{x} \\
&\quad + \sum_{T\in K_{2h,i}}\sum_{\tau\in T} \frac{\partial \zeta_h}{\partial x}\Big|_\tau \int_\tau \varphi_i\phi_j\, d\mathbf{x}, \\
B_{\gamma,2\,ji} &= -\sum_{T\in K_{2h,i}} \frac{\partial \phi_j}{\partial y}\Big|_T \sum_{\tau\in T}\int_\tau H_h\varphi_i\, d\mathbf{x} - \sum_{T\in K_{2h,i}} \frac{\partial H_h}{\partial y}\Big|_T \sum_{\tau\in T}\int_\tau \phi_j\varphi_i\, d\mathbf{x} \\
&\quad + \sum_{T\in K_{2h,i}}\sum_{\tau\in T} \frac{\partial \zeta_h}{\partial y}\Big|_\tau \int_\tau \varphi_i\phi_j\, d\mathbf{x}, \\
B_{\gamma,3\,ji} &= -\gamma \sum_{T\in K_{2h,i}}\sum_{\tau\in T}\int_\tau \varphi_i\phi_j d\mathbf{x}.
\end{aligned}$$

As for (4.15), we choose H_h and z_{bh} linear on each triangle $\tau \in \mathcal{T}_h$ and we use mass lumping

$$\int_\tau H_h\varphi_i d\mathbf{x} = H_i\frac{|\tau|}{3}, \quad \text{and} \quad \int_\tau \varphi_i\phi_j d\mathbf{x} = \frac{|\tau|}{3}\sum_{\mathbf{x}\in\tilde{s}(\tau)} \varphi_i(\mathbf{x})\phi_j(\mathbf{x}),$$

where $s(\tau) = \{v_0, v_1, v_2\}$ are the three vertices of the triangle τ. Finally, the discrete version of the shallow water divergence operator is defined for each vertex of the coarse mesh by $\forall \mathbf{u}_h \in \mathbf{W_h}, \forall j \in \mathcal{J}_M$

$$\mathrm{div}^\gamma_{sw}(\mathbf{u}_h)|_j = \frac{3}{\mathrm{supp}(\phi_j)}\sum_{i\in\mathcal{I}_N}\int_\Omega \mathrm{div}^\gamma_{sw}(\varphi_{\mathbf{i}}(\mathbf{x}))\phi_j(\mathbf{x})\, d\mathbf{x}\, \mathbf{u}_i. \tag{4.17}$$

This definition is used numerically and can be seen as a diagonal preconditioner to solve Eq. (4.14).

5. Numerical algorithm

In this section, we give details about the procedure we use to combine the finite volume method and the finite element method. For the sake of clarity, we just give an overview of the steps of the algorithm. Assuming we know $H^n, H\mathbf{u}^n$, the combined finite volume/finite element method (3.1)-(3.3) can be summarized by the following steps

- Solve the hyperbolic part (3.1) with the finite volume scheme (3.8)-(3.9) and get $(H, H\mathbf{u})^{n+1/2}$. Because of Eq. (3.11), we obtain H^{n+1} as well.
- Solve the elliptic problem (4.14) to obtain p^{n+1}. We use the iterative method described below.
- Update the velocity $\mathbf{u}^{n+1}$ in the correction step (4.11) using $\nabla^\gamma_{sw} p^{n+1}$.

5.1. Iterative methods

The linear problem (4.11)-(4.12) leading to (4.14) is solved in practice with iterative methods. Several algorithms allow us to solve the classical mixed problem (3.15)-(3.16) in the divergence form. This is usually applied to the finite element method for the Navier-Stokes equations, see [52, 41]. We describe here the Conjugate Gradient method (CG) and the Uzawa algorithm (see [45, 52]) which uses the duality property of the operators. In practice, to take the boundary conditions into account, the matrix consists in two blocks in which one part contains the elements of $B_\gamma A_H^{-1} B_\gamma^T$ for all the nodes that have to be solved and another diagonal part which is the identity and corresponds to impose

Dirichlet conditions for the pressure. Then the contribution of the matrix B_γ associated with the given pressure is affected on the right hand side. The linear problem can be written

$$\begin{pmatrix} \mathcal{A} & 0 \\ 0 & Id \end{pmatrix} P = \begin{pmatrix} \frac{1}{\Delta t}\mathcal{D} - \mathcal{A}_G P_G \\ P_G \end{pmatrix}, \tag{5.1}$$

where $\mathcal{A}$ is the matrix extracted from $B_\gamma A_H^{-1} B_\gamma^T$ corresponding to the fact that we restrict to the nodes of unknowns, respectively $\mathcal{A}_G$ to the nodes of the given pressure P_G. The matrix $\mathcal{D}$ is the shallow water divergence vector of the velocity at the unknown nodes at the prediction part. This reduces the size of the problem and allows us to apply the Conjugate Gradient algorithm. The initialization is done with the state $(Hu, Hv, Hw)^{n+1/2}$ computed at the hyperbolic step. For the sake of clarity, we drop the superscripts $^{n+1/2}$ and we denote with the superscript $^{(k)}$ the index iteration of the iterative method. In addition, we use the notation $f = \frac{1}{\Delta t}\mathcal{D} - \mathcal{A}_G P_G$. Then the CG algorithm can be summarized as:
Initialization

$$\begin{aligned} &U^{(0)}, P^{(0)} \text{ given}, \\ &r^{(0)} = f - \mathcal{A}P^{(0)}, \\ &d^{(0)} = r^{(0)}. \end{aligned}$$

For $k > 0$

$$\begin{aligned} \rho &= \frac{(r^{(k)}, d^{(k)})}{(d^{(k)}, \mathcal{A}d^{(k)})}, \\ P^{(k+1)} &= P^{(k)} + \rho d^{[k)}, \\ r^{(k+1)} &= r^{(k)} - \rho \mathcal{A} d^{(k)}, \\ \delta^{(k+1)} &= \frac{||r^{(k+1)}||^2}{||r^{(k)}||^2}, \\ d^{(k+1)} &= r^{(k+1)} + \delta^{(k+1)} d^{(k)}. \end{aligned}$$

Then, the correction is applied to the velocity.

For the description of the Uzawa method, let us now use the duality between the operators (3.4) and (2.33), keeping the notations

$$\begin{aligned} &U^{(0)}, P^{(0)} \text{ given}, \\ &P^{(k+1)} = P^{(k)} + \alpha B_\gamma U^{(k)}, \\ &A_H U^{(k+1)} = A_H U^{n+1/2} - \Delta t B_\gamma^T P^{(k+1)}, \end{aligned}$$

with α chosen such that $0 < \alpha < \frac{2}{\max \lambda_i}$ with λ_i the eigenvalues of $B_\gamma A_H^{-1} B_\gamma^T$. The CG algorithm adapted for problem (4.11)-(4.12) in the form of the Uzawa algorithm reads:
Initialization

$$\begin{aligned} U^0 &= U^{n+1/2}, \\ d^{(0)} &= r^{(0)} = B_\gamma U^{(0)}, \end{aligned}$$

$k > 0$

$$\alpha^{(k)} = \frac{(r^{(k)}, d^k)}{(B_\gamma^T d^{(k)}, A_H^{-1} B_\gamma^T d^{(k)})},$$

$$P^{(k+1)} = P^{(k)} + \alpha^{(k)} d^{(k)},$$
$$Z = A_H U^{n+1/2} - \Delta t B_\gamma^T P^{(k+1)}.$$

Solve the system $A_H U^{(k+1)} = Z$ (we recall that the matrix A_H is diagonal since we have used mass lumping).
Compute $B_\gamma U$

$$r^{(k+1)} = B_\gamma U^{(k+1)},$$
$$\delta^{(k+1)} = \frac{||r^{(k+1)}||^2}{||r^{(k)}||^2},$$
$$d^{(k+1)} = r^{(k+1)} + \delta^{(k+1)} d^{(k)}.$$

In accordance with Eqs. (4.16),(4.17), the norm $||.||$ used in the above iterative algorithms takes into account the normalization of the operators by the basis function support area.

5.2. **Wet-dry interface**

As one can see, the method presented above supposes that the water depth does not vanish since the resolution of the pressure equation (3.4) requires dividing the shallow water gradient by H. At the discrete level, this difficulty arises in the mass matrix (4.13). But in practice, it is necessary that the model be able to capture dry/wet interfaces e.g. when considering wave propagation over obstacles like islands or reaching a coast line.

In practice, we introduce a small parameter ε such that the pressure equation (3.4) returns $p = 0$ when H tends to zero. This can be viewed as a Dirichlet condition on the dry zone of the domain, such that the pressure equation is solved only on the wet domain. In the iterative solver, this leads to testing the value of the water depth for each node s_j of the mesh (or for the coarse mesh if the P_1-isoP_2/P_1 approximation is used). However, in order to avoid selecting a list of dry nodes at each time step, which would require significant computation time, we solve the whole problem and we introduce a threshold

$$\varepsilon \ll 1, \tag{5.2}$$

under which the water depth is redefined by ε, namely $H_\varepsilon = \max(H, \varepsilon)$. Since the mass matrix M_H is weighted with H and needs to be inverted in the correction step, to avoid having singularities, the matrix is redefined with respect to H_ε as

$$M_{H_\varepsilon ji} = \sum_{T \in K_{h,i}} \int_T H_\varepsilon \varphi_i \varphi_j d\mathbf{x}.$$

Then, at the correction step, the shallow water gradient is redefined by

$$\nabla_{sw}^{\gamma,\varepsilon} p|_i = \frac{\mathbb{1}_{H_i > H_\varepsilon}}{\text{supp}(\varphi_i)} \sum_j \int_\Omega \nabla_{sw}^\gamma (\varphi_j) \cdot \varphi_i d\mathbf{x}\, p_j, \tag{5.3}$$

so the velocity is not updated at these nodes by step (3.2). In Eq. (5.3), the function φ_j is replaced by ϕ_j if we use P_1-isoP_2/P_1 space approximation. Notice that introducing H_ε does not change the result since it appears only in the terms of degree zero for the derivative of the pressure. It only prevents from redefining wet/dry zones at each iteration. With these definitions, the Laplacian operator written in (3.5) becomes

$$\Delta_{sw}^{\gamma,\varepsilon} p = \text{div}_{sw}^\gamma \left(\frac{\nabla_{sw}^\gamma}{H_\varepsilon} p \right) = \nabla_{x,y}.(H \nabla_{x,y} p) + \left(\Delta\zeta - \frac{1}{H_\varepsilon} \left(\left(\frac{\partial \zeta}{\partial x} \right)^2 + \left(\frac{\partial \zeta}{\partial y} \right)^2 + \gamma^2 \right) p \right). \tag{5.4}$$

5.3. **Toward second order schemes**

For the fully discrete scheme (3.8)-(3.14), a first order time discretization has been presented but a second order extension based on the Heun scheme [16] – that is a slight modification of the second order Runge-Kutta method – has been implemented and is used in the simulations proposed in the next section. More precisely, we use a modified version of the Heun scheme that allows to preserve invariant domains, typically the non-negativity of the water depth, see [3, paragraph. 5.8.2] for a complete description of the Heun scheme and its modified version.

We also extend to a formally second-order approximation the space discretization of the prediction step (3.8)-(3.9) using a MUSCL like extension (see [55]). More precisely, we replace the piecewise constant values $X_i^{*,n}, X_j^{*,n}$ in the numerical flux of Eqs. (3.8)-(3.9) by more accurate reconstructions deduced from piecewise linear approximations, namely the values $X_{i,j}^{*,n}, X_{j,i}^{*,n}$ reconstructed on both sides of the interface. The reconstruction procedure is similar to the one used and described in Section 5.1 from [7].

In [3] the second order extensions in space and time are confronted with non-stationary analytical solutions. Since when a single layer is considered, the model in [3] reduces to the classical Saint-Venant system, the results in [3] highlight the benefits of these extensions for the approximation of the hyperbolic part of the dispersive model considered in this paper.

Notice that several implementations of the projection-correction scheme are available, see [39]. The authors have also tested the incremental version proposed in [39], this does not modify the obtained order of convergence of the scheme for the analytical test cases presented in paragraphs 6.1 and 6.2.

6. **Numerical validation**

In this section, we confront the numerical procedure with several test cases. First, we present convergence curves for two time dependent analytical solutions allowing to validate the numerical resolution. Then comparisons with experimental data and in the situation of an earthquake-generated tsunami are performed enforcing the validity of the model. From some of the analytical and experimental test cases, we investigate the influence of the chosen value for the parameter γ.

6.1. **A solitary wave**

The solitary wave is a one-dimensional non-stationary analytical solution of the model. This solution has been proposed to validate the one-dimensional model in [2] and has the form

$$H = H_0 + a\left(\operatorname{sech}\left(\frac{x - c_0 t}{l}\right)\right)^2,$$

and we deduce

$$u = c_0\left(1 - \frac{d}{H}\right), \quad w = -\frac{c_0 d}{\gamma}\frac{\partial(\ln H)}{\partial x},$$
$$p = -\frac{c_0 d H}{\gamma^2}\left(\frac{\partial^2(\ln H)}{\partial x \partial t} + c_0\left(1 - \frac{d}{H}\right)\frac{\partial^2(\ln H)}{\partial x^2}\right),$$

with $d, a, H_0 \in \mathbb{R}$, $H_0 > 0$, $a > 0$ and $c_0 = \frac{H_0}{d}\sqrt{g(H_0 + a)}$, $l = \frac{2H_0}{\gamma}\sqrt{\frac{H_0}{a} + 1}$.
This analytical solution is extended to two dimensions in a rectangular channel and the definition $v = 0$ is added to the previous equations.
We consider a channel of dimension 30 m $\times$1 m, the water elevation H_0 is set to 1 m with significant wave amplitude $a = 0.35$m and $d = 1$m. On the model domain in Figure 2.1, we set a slip boundary condition for Γ_s, a given discharge for the inlet (2.8) and a water elevation at the outlet (2.9) with

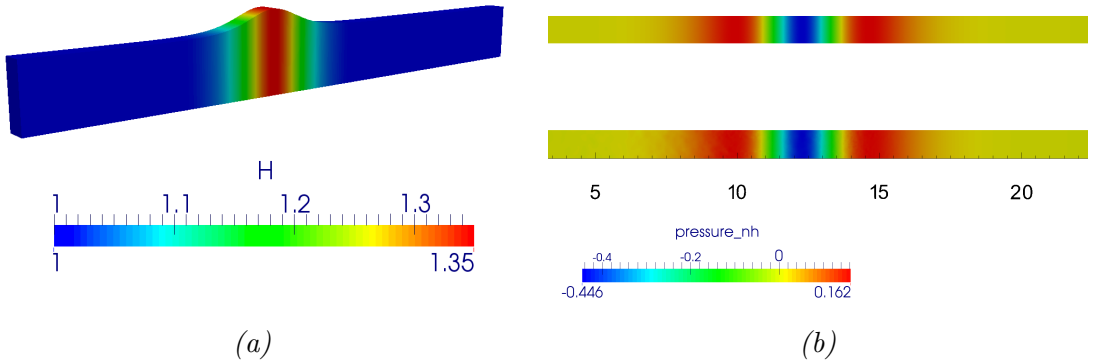

FIGURE 6.1. Illustration of the solitary wave propagation at $t = 1.99$ s, *(a)* computed water depth (lateral view) and *(b)* non-hydrostatic pressure (top view), analytical solution at the top, numerical field below.

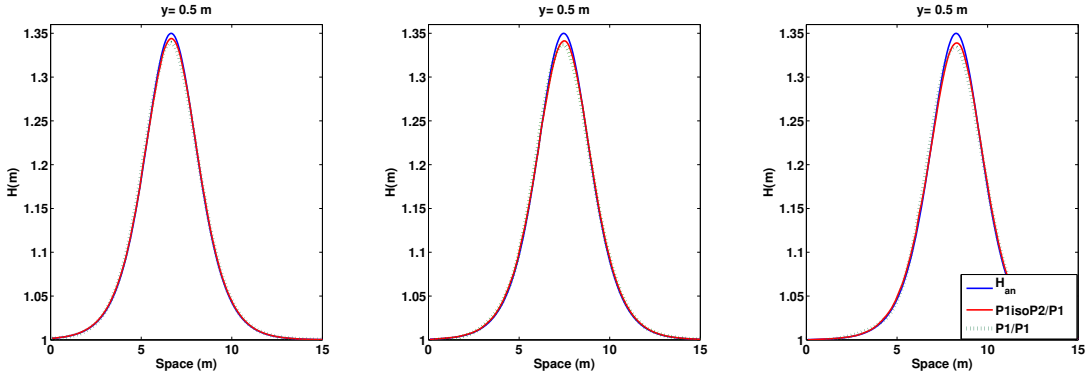

FIGURE 6.2. Comparison between the analytical water depth H_{an} and the P_1isoP$_2$/P_1 and the P_1/P_1 approximations on the solitary wave propagation.

a homogeneous Dirichlet boundary condition for the pressure at the correction step. The test case is initialized with the analytical solution in the domain and we observe the propagation of the wave over time.

In Fig. 6.1, we show the computed water depth (Fig. 6.1-*(a)*) and the computed and analytical pressures (Fig. 6.1-*(b)*). Notice that the numerical results have been obtained for $\gamma = 2$ but since it is an analytical solution, any other choice for γ would have given the same results. This has been obtained with the P_1-isoP$_2$/P_1 approximation and the wave has covered approximately one wavelength.

A numerical comparison of the P_1/P_1 and P_1-isoP$_2$/P_1 approximations is proposed in order to choose the most accurate one for practical applications. In Fig. 6.2, we compare the numerical solutions, computing the P_1/P_1 solution on the fine mesh of the P_1-isoP$_2$/P_1, here an unstructured mesh of 72770 nodes. After a short time, the P_1/P_1 method provides a less accurate solution than the P_1-isoP$_2$/P_1

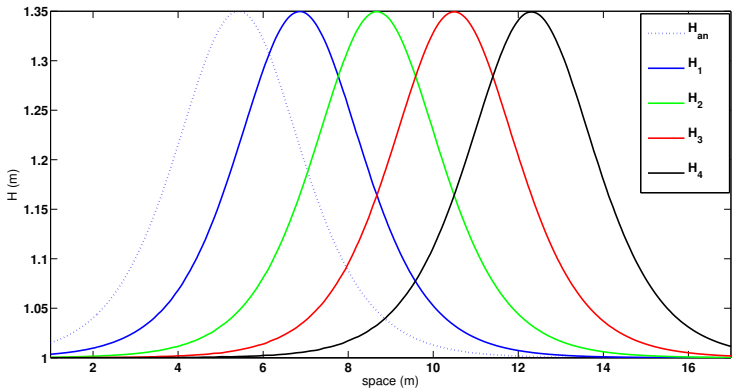

FIGURE 6.3. Cross section at the center of the channel $y = 0.5$ m; water depth of the analytical solution at initial time $H_0 = H_{an}$ and computed solution $H(t_i), i = 1, \ldots, 4$ with $t_0 = 0$ s, $t_1 = 0.499805$ s, $t_2 = 0.999871$ s, $t_3 = 1.49983$ s, $t_4 = 1.99993$ s for the P_1-isoP$_2$/P_1 approximation and the improved method (Heun scheme).

approximation, since we observe the amplitude of the wave obtained by the P_1-isoP$_2$/P_1 method is closer to the analytical solution than the P_1/P_1 approximation.

Since the comparison gives better results with the P_1-isoP$_2$/P_1 spaces, we opt for this approximation to validate the method. We apply the "improved" method presented in paragraph 5.3 and obtain a good approximation of the soliton during all the propagation (see Fig. 6.3), we observe that the solitary wave preserves its amplitude over the time. The simulation shown in Fig. 6.3 was computed with 251330 nodes for the fine mesh. We study the convergence rate of the computed solutions, computing the L^2 error at time $t = 1.99$ s for different meshes corresponding to a triangulation with mean edges $h_0 = 0.0493528$ m, $h_1 = 0.0250468$ m and $h_2 = 0.016781$ m. Figure 6.4 shows the logarithm of the L^2 error between the analytical solution and the numerical solution with respect to $\log\left(\frac{h_0}{h}\right)$ where $h = h_i, i = 0, 1, 2$. We observe a convergence rate close to 1 for the first order method, while with the improved scheme we still obtain approximately a first order convergence rate, although the computed error is smaller.

Notice that the simulations have also been carried out when, at the initial instant, the soliton is outside of the considered domain. The simulation results and the convergence curve are exactly the same, see [2]. It is a good indicator of the quality of the numerical treatment of the boundary conditions.

6.2. **A periodic analytical solution with wet-dry interfaces**

In this section the objective is to validate the method with a non stationary analytical solution where the free surface oscillates over the time. Such solutions have been introduced by Thacker in [54] for the shallow water equations and can be obtained over a paraboloid topography with a velocity (u, v) varying only with respect to time. In the following proposition, we extend the result proposed by Thacker to the case of the non-hydrostatic model (2.29)-(2.31).

Proposition 6.1. *Let $H_0 \in \mathbb{R}_+$, $(a, b) \in \mathbb{R}^2$ with $|ab| \leq 1$ and*

$$\omega^2 = \frac{ag}{1 - a^2b^2}.$$

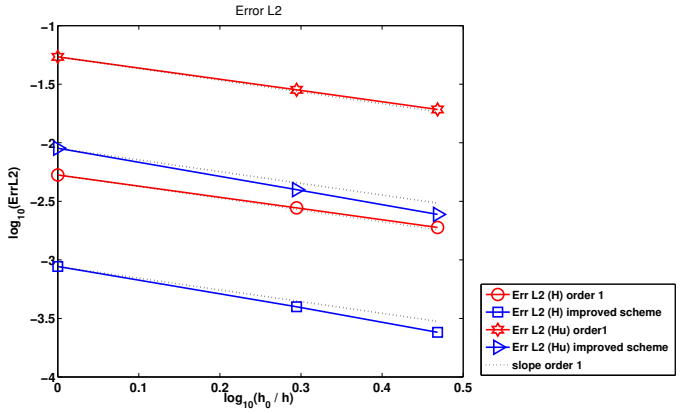

FIGURE 6.4. Convergence rate for the P_1-isoP_2/P_1 approximation for the classical scheme (order 1 in time and space) and the improved method (Heun scheme and reconstruction in the prediction step). The L^2 error is computed at time $t = 1.99s$

.

Then the functions H, u, v, w, p, s defined by

$$H(x,y,t) = \max\left(0, H_0 - \frac{a}{2}\left(x - b\cos(\omega t)\right)^2 - \frac{a}{2}\left(y - b\sin(\omega t)\right)^2\right),$$
$$u(x,y,t) = -b\omega\sin(\omega t), \quad v(x,y,t) = b\omega\cos(\omega t), \quad w(x,y,t) = -ab\omega(\sin(\omega t)x - \cos(\omega t)y),$$
$$p(x,y,t) = \frac{b^2 a\omega^2}{2} H(x,y,t),$$
$$s(x,y,t) = ab\omega^2(\sin(\omega t)x - \cos(\omega t)y),$$

with the topography

$$z_b(x,y) = a\frac{x^2+y^2}{2},$$

are solution of the model

$$\frac{\partial H}{\partial t} + \nabla_0 \cdot (H\mathbf{u}) = 0,$$
$$\frac{\partial (H\mathbf{u})}{\partial t} + \nabla_0 \cdot (H\mathbf{u}\otimes\mathbf{u}) + \nabla_0(\frac{g}{2}H^2) + \nabla_{sw}^{\gamma} p = -gH\nabla_0(z_b) + S,$$
$$\mathrm{div}_{sw}^{\gamma}(\mathbf{u}) = 0,$$

with $S = (0,s)^T$ corresponding to the model (2.29)-(2.31) *with $\gamma = 2$ and where* (2.30) *is completed with the source term S.*

Proof. []Proof of prop. 6.1. The proof relies on simple computations and is not detailed here. ∎

Remark 6.2. The proposition 6.1 is valid only for $\gamma = 2$, see also [21]. And it is worth noticing that, as proved in [21], the solution proposed in prop. 6.1 is also an analytical solution for the full Euler system (2.11)-(2.12),(2.13)-(2.15). Thus the model $\mathcal{M}_2$ shares common analytical solutions with the Euler system, this has already been mentioned (see paragraph 2.4.2).

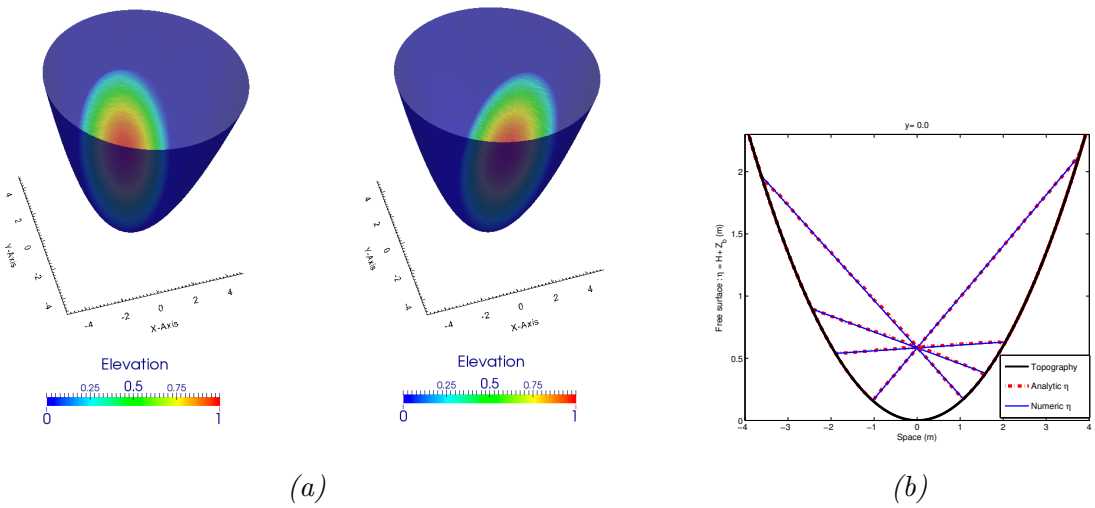

(a) *(b)*

FIGURE 6.5. *(a)* Simulation of the free surface oscillations in a paraboloid at different time steps and *(b)* cross section of the free surface at $y = 0$ of the free surface $H + z_b$ compared with the analytical solution at different times: $t_0 = 0.277222$ s, $t_1 = 0.431123$ s, $t_2 = 0.739382$ s, $t_3 = 0.893419$ s ans $t_4 = 1.20134$ s.

We run this test on a disc domain centered in $(x, y) = (0, 0)$ with a radius of 5 m, with $a = 0.3$ m^{-1}, $b = 1.6$ m and $H_0 = 1.0$ m as shown in Figure 6.5-*(a)*. This case is simulated with 440746 nodes for the fine mesh (and 220588 for the coarse mesh). We use the strategy proposed in paragraph 5.2 to treat the wet-dry front with ε defined by (5.2), $\varepsilon = 10^{-5}$ m and we impose a discharge equal to zero at the boundary conditions (2.8) and a Dirichlet boundary condition for the pressure on Γ. In Fig. 6.5-*(a)*, the representation of the free surface oscillating in the bowl is shown for different time steps. Figure 6.5-*(b)* presents the profile of the elevation in the cross-section $y = 0$ at different time steps compared with the analytical solution. This is a crucial test case for the validation of the method since we test the dry/wet - wet/dry transitions and strong variations of the free surface. We also compute the convergence rate with the same formula described for the solitary case (see paragraph 6.1) for different meshes where $h_0 = 0.0551138$ m, $h_1 = 0.0412458$ m, $h_2 = 0.0330043$ m, $h_3 = 0.0274674$ m, where h_i, $i = 0, \ldots, 3$ are the mean edges of the meshes. In Fig. 6.6, we observe that the convergence rate is close to one for the water depth, the vertical discharge Hw and the non-hydrostatic pressure p. These simulated results are computed with the improved method described in 5.3 and as expected, we obtain a similar slope for Hw and p and a better convergence for H which is not corrected in the second step of the scheme (3.2).

6.3. **Dingemans experiments - effect of the choice of γ**

The experiments carried out by Dingemans [27] at Delft Hydraulics deal with the wave propagation over uneven bottoms. A small amplitude wave (0.02 m) is generated at the left boundary of a closed basin with vertical shores. At rest, the water depth in the channel varies from 0.4 m to 0.1 m, see Fig. 6.7. Eight sensors recording the free surface elevation are located at abscissa 2 m, 4 m, 10.5 m, 12.5 m, 13.5 m, 14.5 m, 15.7 m and 17.3 m.

Since the studied model (2.29)-(2.31) depends on a parameter γ, we have tried to investigate the impact of the parameter value. The value $\gamma = \sqrt{3}$ – corresponding to the Green-Naghdi model – and

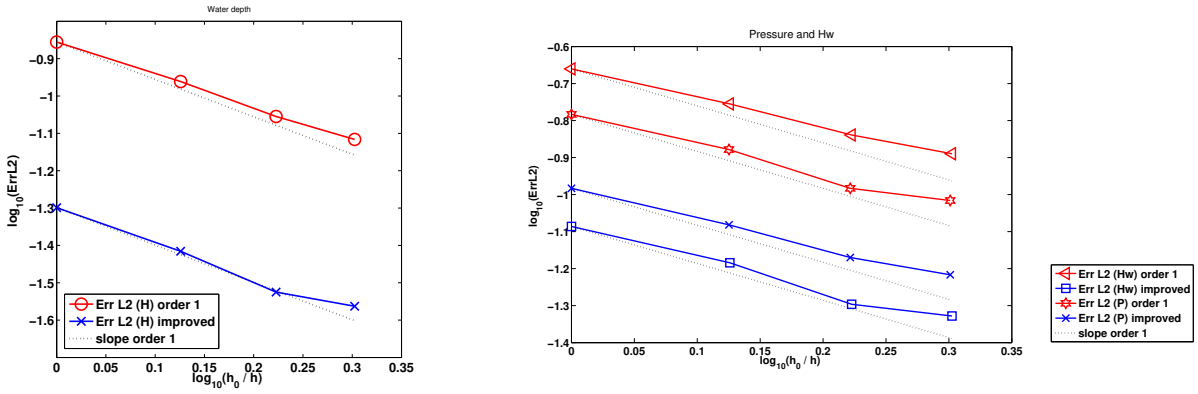

(a) *(b)*

FIGURE 6.6. Convergence rate: *(a)* of the L^2 error of the water depth and *(b)* of the vertical discharge and the pressure.

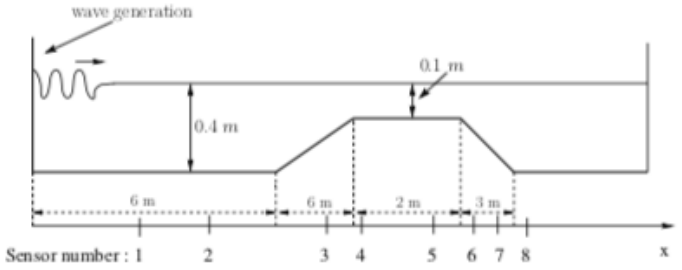

FIGURE 6.7. Channel profile for the experiments and location of the sensors.

the value $\gamma = 2$ – corresponding to the model proposed by some of the authors – have been tested and the simulation results are depicted in Figs. 6.7.

It appears over Figs. 6.8 that either for $\gamma = 2$ or for $\gamma = \sqrt{3}$, the simulation results are rather in good agreement with the recorded data. Nevertheless, we can see over Figs. 6.8 that the Green-Naghdi model i.e. when $\gamma = \sqrt{3}$ gives better results than the model for $\gamma = 2$. This is in accordance with the fact that the Green-Naghdi model is well adapted for gravity wave propagation whereas for advection dominated flows, the value $\gamma = 2$ can be singled out, see remark. 6.2.

Remark 6.3. The values $\gamma = 2$ and $\gamma = \sqrt{3}$ corresponding to existing models are mainly used. It is important to notice that in the case of the Dingemans experiments, with values of γ very different from 2 and $\sqrt{3}$ e.g. $\gamma = \sqrt{5}$, the obtained results are worse but not significantly different, see Fig. 6.9.

6.4. **Application to the 2014 Iquique earthquake, Chile**

In this section we apply the depth-averaged model (2.29)-(2.31) to a real geophysical event i.e. an earthquake-generated tsunami. On April 1, 2014 at 23:46:47 UTC, a 8.2 magnitude earthquake struck off the coast of northern Chile and generated a tsunami. The earthquake was localized at 95km NW of Iquique (see Figure 6.10) and the elevation of the water depth was recorded by the Deep-ocean

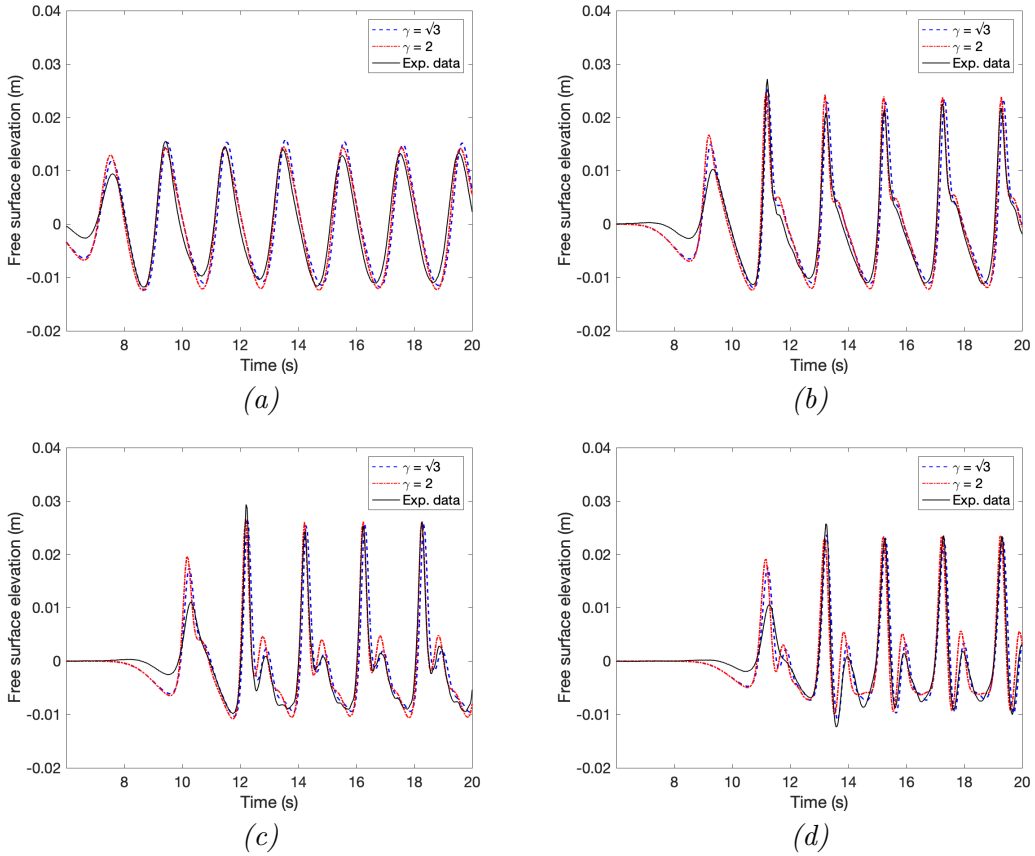

FIGURE 6.8. Comparisons between the experimental data (solid line) and the simulations of the dispersive model with $\gamma = \sqrt{3}$ (blue dashed line) and $\gamma = 3/2$ (red dashed-dotted line). Figs. *(a)*, *(b)*, *(c)* and *(d)* respectively correspond to the results for the sensors 3, 4, 5 and 6.

Assessment and Reporting of Tsunamis (DART) buoys of the NOAA center for tsunami research [10]. The objective of this section is to confront the results of the hydrostatic and non-hydrostatic shallow water models to the water wave measurements of the DART buoys. To simulate the tsunami generated earthquake, we use a topography given by the NOAA and consider two different sources, denoted by Source A and Source B, describing the displacement of the topography during the earthquake (see Fig. 6.11). These sources have been chosen because of their different spatial variability: source A is overall more symmetric and smoother than source B (Fig. 6.11). Since dispersive effects are expected to be more important for shorter wavelength spatial heterogeneities, we investigate here the relative importance of dispersive effects for these two sources. In particular, we compare the simulations using both the hydrostatic and non-hydrostatic models on two gauges represented in Figure 6.12-*(a)* and corresponding to the location of

- the closest DART buoy: DART-32401 localized at 260 NM West-Southwest of Arica, Chile at Latitude/Longitude coordinates (-20.473, -73.429).
- a point denoted S, localized at coordinates (-21.98702, -71.14027), closer to the coast and next to the trench where bathymetry variations are huge.

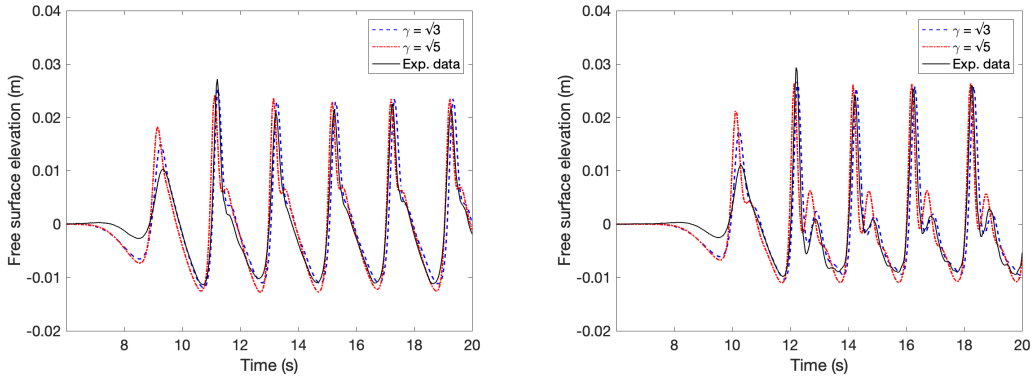

FIGURE 6.9. Comparisons between the experimental data (solid line) and the simulations of the dispersive model with $\gamma = \sqrt{3}$ (blue dashed line) and $\gamma = \sqrt{5}$ (red dashed-dotted line). Figs. *(a)*, *(b)* respectively correspond to the results for the sensors 4 and 5.

The simulation is made on a spatial domain covering an area of 800 km × 1200 km (Fig. 6.10 and 6.12). For the initial conditions, we prescribe (i) a horizontal free surface for the water and (ii) the bathymetry before the earthquake occurred (Fig. 6.12). The topography associated with the unstructured mesh is obtained by a linear interpolation of the ETOPO1 Arc-Minute Global Relief Model [5]. According to the comments in paragraph 2.4.2 and the results obtained in paragraph 6.3, the value $\gamma = 2$ has been chosen for the simulations. Notice that with $\gamma = \sqrt{3}$, the simulation results are very similar in the sense that the differences cannot be seen with the naked eye.

The initial instant of the simulation exactly corresponds to the trigger point of the seism. The earthquake is simulated by updating the bathymetry at the first time step. The imposed bottom displacement is illustrated in Figure 6.11 for sources A and B. For the non-hydrostatic simulation, the fine mesh – on which the velocity is computed – has 470174 nodes which gives a size of triangle edges of about 2.5 km, while the coarse mesh - on which the pressure is computed - has 117088 nodes. The hydrostatic simulation has been performed on the fine mesh. We use the improved method with second order of accuracy in time and space for both simulations.

Figure 6.13 shows that non-hydrostatic effects generate waves with higher frequencies, as expected. In Fig. 6.14-A, we compare the simulated water waves obtained with source A using the hydrostatic and non-hydrostatic models with the waves recorded at the DART buoy 32401. The simulation pretty well reproduces the first wave in terms of amplitude and phase. The higher frequency oscillations of the water surface are not at all captured by the hydrostatic model (dashed line). These oscillations may result from more complex effects like dispersion. The non-hydrostatic (DAE) model produces indeed higher frequencies than the hydrostatic model. However these higher frequency oscillations are very small compared to the observed ones. As a result, in this case, the dispersion effects do not seem to play a significant role.

In Fig. 6.14-B, we do the same comparison with simulations based on the more heterogeneous source B. Although the simulated maximum amplitude and the phase of the first wave are further from the observation, the differences between the hydrostatic and non-hydrostatic models are larger. In particular, the non-hydrostatic model generates an oscillation at higher frequency (between times around 1.734 s and 1.737 s) followed by smaller fluctuations. This oscillation bears some similarities

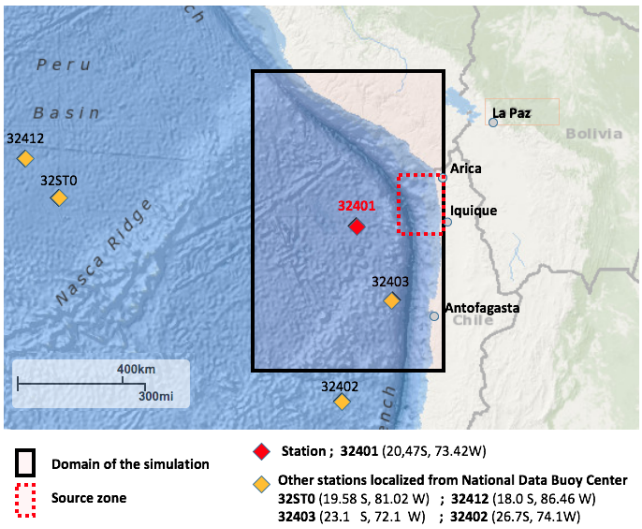

FIGURE 6.10. Map of the Chilean coast with localization of the simulated domain. Localization of the DART buoy 32401 and the other reference DART buoys (see NOAA's data).

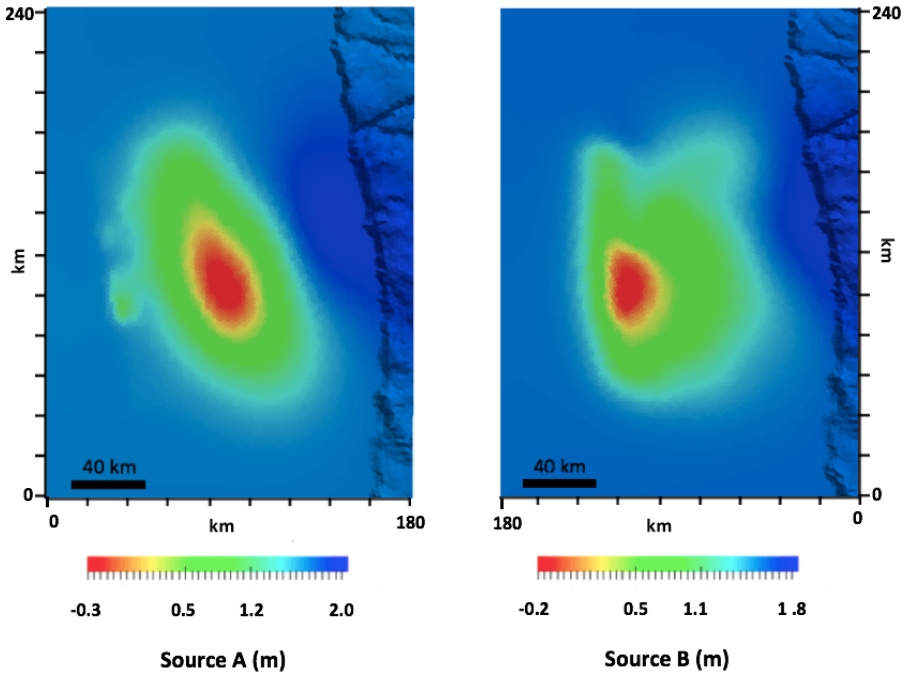

FIGURE 6.11. Imposed displacement for (a) source A and (b) source B. The selected zone corresponds to the source zone in red shown in Fig. 6.10.

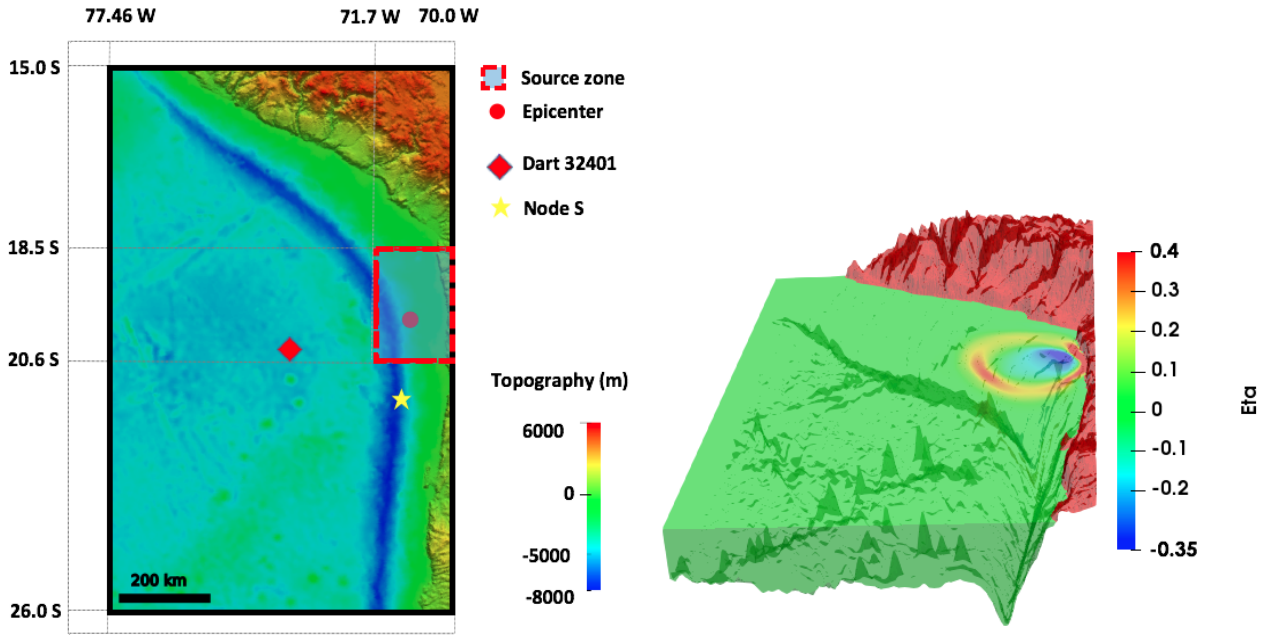

FIGURE 6.12. *(a)* Topography and bathymetry of the simulation domain (Chile) and location of the earthquake epicenter, the DART buoy 32401 and the gauge S. *(b)* Simulated free surface variation η of the tsunami wave at time 666 s.

with the oscillation that follows the first wave in the observations (between times around 1.735 and 1.738 s), even though the phase is different and the amplitude of the negative part is smaller than the recorded wave.

The ability of the DAE model to generate higher frequencies is illustrated on the waves simulated at gauge S for the two sources (Fig. 6.15). At this location, there are strong gradients of the bathymetry (see Fig. 6.12-*(a)*), that are expected to enhance non-hydrostatic effects. We observe indeed that at this location, dispersive effects are more important for both sources and produce high frequency oscillations. Interestingly, the two sources give very different high frequency waves, suggesting that detailed comparison between simulation and observation in this frequency range may provide insight into the source heterogeneity, provided non-hydrostatic effects are properly accounted for. Further investigation of the impact of detailed source characteristics on high frequency waves would be very interesting but beyond the scope of this paper. A big issue is the numerical cost of such non-hydrostatic simulations making it difficult to perform sensitivity analysis since a very fine mesh is required to obtain converged numerical solutions.

7. Conclusion

In this paper, we have presented a new method for a family of two-dimensional dispersive shallow water systems, where we do not solve equations containing high order derivatives but a mixed problem in velocity and pressure. This allows to apply the method with appropriate boundary conditions for the velocity and the pressure, which is usually a difficult task when high order equations are solved. In addition, due to the general framework of the method and the definition of the shallow water operators, i.e. the duality property on which the method is based, the algorithm has been applied on unstructured meshes using a combined finite volume / finite element method to solve a hyperbolic system on the one hand and an elliptic equation on the other hand. The algorithm uses an iterative method of Uzawa

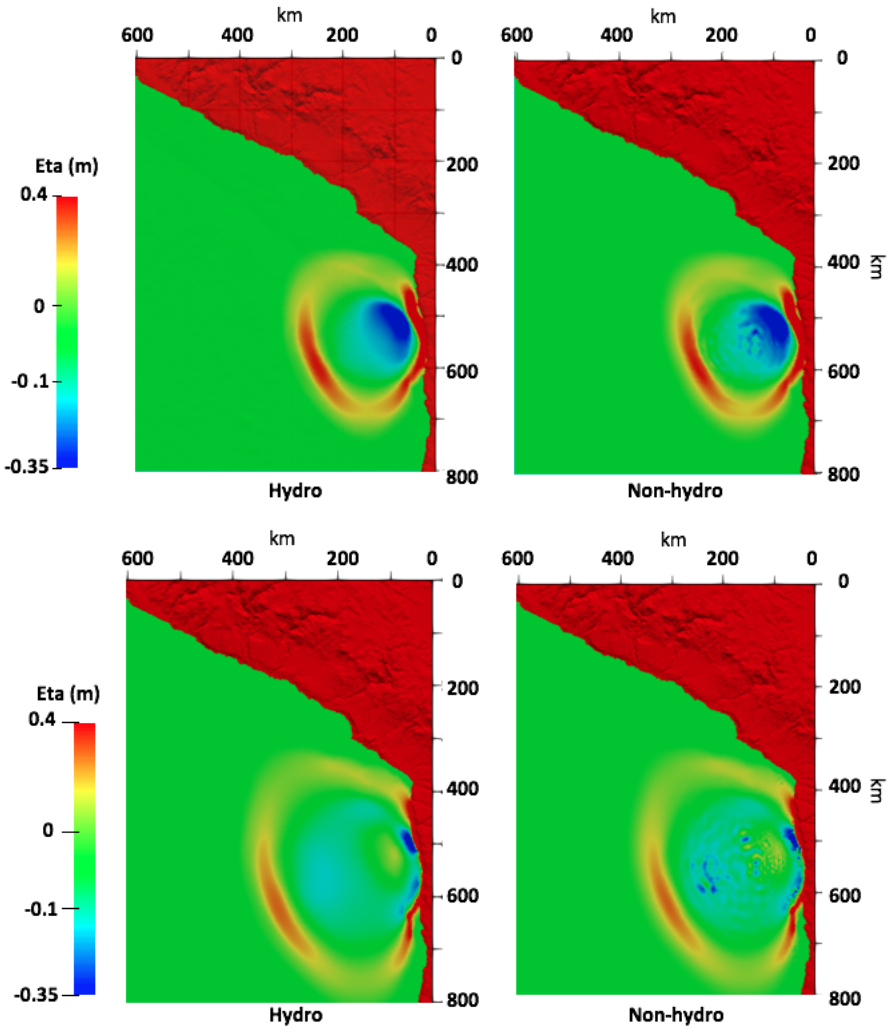

FIGURE 6.13. Comparison of the wave front for the hydrostatic (left) and the non-hydrostatic (right) model at time $t = 666$ s (upper part) and $t = 999$ s (lower part) and using the source A. The coordinate (0,0) corresponds to the coordinate (15.0 S, 70.0 W).

type to solve the elliptic problem. We provide a numerical validation with two analytical solutions. We have proved that our model is applicable at the scale of geophysical events by simulating an earthquake generated tsunami in Chile. Our simulations pretty well reproduce the recorded wave. Our results show that, in a real situation, strong differences may be obtained between hydrostatic and non-hydrostatic simulations, depending on the variability of the topography around the recorded gauge and on the source heterogeneity. Interestingly, the two different sources investigated here give very different high frequency oscillations suggesting that a detailed comparison between simulation and observation in this frequency range may give insight into the source heterogeneity, providing non-hydrostatic effects are accurately accounted for. And such a sensitivity to the bottom topography variations implies to work with fine spatial discretizations increasing significantly the computational costs and the need of an optimized resolution of the elliptic step that has not been studied in this paper.

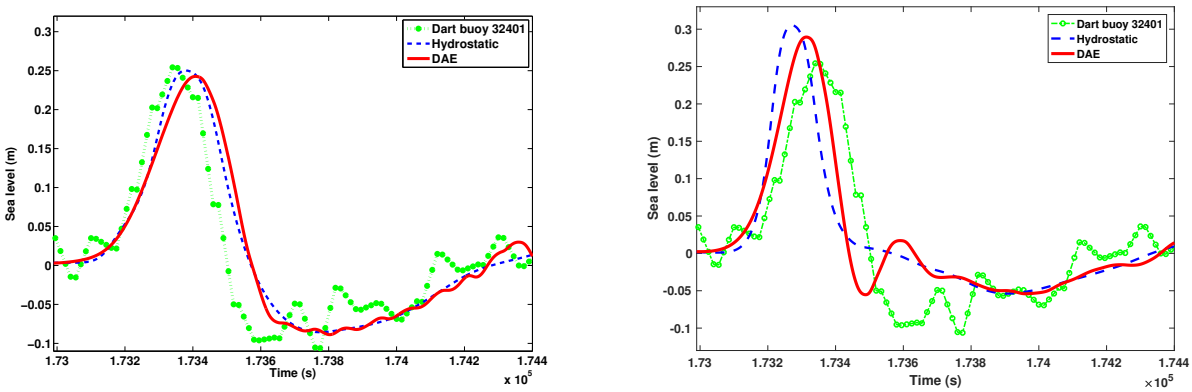

Source A Source B

FIGURE 6.14. Comparison between numerical results using both models (hydrostatic and non-hydrostatic) and the data of the DART buoy 32401 for (a) source A and (b) source B.

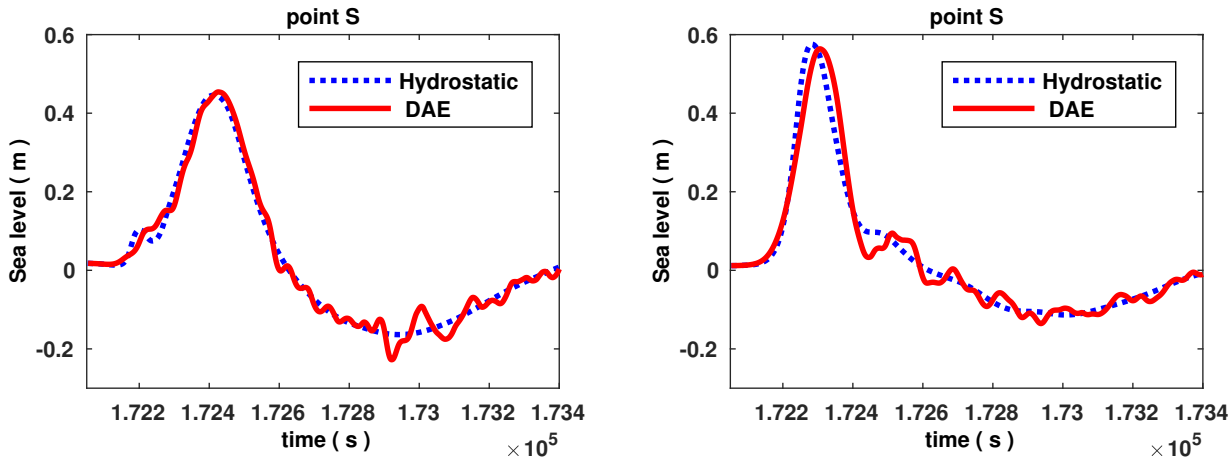

Source A Source B

FIGURE 6.15. Comparison between numerical results using both models (hydrostatic and non-hydrostatic) at the node S for (a) source A and (b) source B.

Indeed, compared to classical finite volume schemes for the approximation of the shallow water equations, the proposed strategy for the resolution of these dispersive models only add the resolution of a linear elliptic-type equation. Nevertheless, the iterative inversion of the elliptic operator does increase the computational costs and an optimized technique e.g. using a preconditioning is required. In order to reduce the computational costs, the authors have recently proposed a relaxed version of the dispersive model studied in this paper where the elliptic equation can be solved using an explicit time scheme, see [26]. Besides, some of the authors are currently working on the extension of the proposed numerical strategy to layer-averaged approximations of the 3d Euler system [32].

Acknowledgments

The authors thank Robert Eymard for his helpful and constructive discussions that greatly contributed to improve the final version of the paper and Martin Vallée, Sebastien Allgeyer and Raphaël Gradin for providing the inverted sources for the tsunami simulation and for fruitful discussions. The authors acknowledge the Inria Project Lab Algae in Silicio for its financial support. The first author received a partial grant from the Fondation Ledoux. This research is also supported by the ANR MIMOSA project and the ERC SLIDEQUAKES ERC-CG-2013-PE10-617472.

Appendix A. Equivalence with the Green-Naghdi system

In this section, we prove the equivalence up to some second order error terms between the formulation (2.1)-(2.5) and the Green-Naghdi system described in [43, 15, 44] i.e. we generalize [46] (see also [21, paragraph 3.4]) to the 2d case and with a non flat topography.

Following the formulation given in [44, paragraph 2.1] (see also [15]), the Green-Naghdi system writes

$$\frac{\partial H}{\partial t} + \nabla_{x,y}.(HU) = 0, \tag{A.1}$$

$$(1 + \mu\mathcal{T}[H, z_b]) \left(\frac{\partial U}{\partial t} + (U.\nabla_{x,y})U \right) + g\nabla_{x,y}(H + z_b) + \mu\mathcal{Q}[H, z_b]U = 0, \tag{A.2}$$

with $U = (u, v)$ and

$$\mathcal{T}[h, z]W = \mathcal{R}_1[h, z](\nabla_{x,y}.W) + \beta\mathcal{R}_2[h, z](\nabla_{x,y}z.W),$$

$$\mathcal{Q}[h, z]W = -2\mathcal{R}_1[h, z]\big(\partial_x W.\partial_y W^{\perp} + (\nabla_{x,y}.W)^2\big) + \beta\mathcal{R}_2[h, z]\big(W.(W.\nabla_{x,y})\nabla_{x,y}z\big),$$

where $W^{\perp} = (-W_2, W_1)^T$ if $W = (W_1, W_2)^T$ and

$$\mathcal{R}_1[h, z]f = -\frac{1}{3h}\nabla_{x,y}(h^3 f) - \beta\frac{h}{2}f\nabla_{x,y}z,$$

$$\mathcal{R}_2[h, z]f = \frac{1}{2h}\nabla_{x,y}(h^2 f) + \beta f\nabla_{x,y}z. \tag{A.3}$$

Notice that in the previous equations and as in [44, paragraph 2.1], the parameter μ corresponds to the shallowness of the flow while β accounts for the amplitude of the topography variations.

The two models (2.1)-(2.5) and (A.1)-(A.2) correspond to shallow water flows and hence are mainly valid in the context of $\mu, \beta \ll 1$. The following proposition holds.

Proposition A.1. *Up to $\mathcal{O}(\mu\beta^2)$ terms, the model* (2.1)-(2.5) *with $\delta = 3/2$ (or the model* (2.24)-(2.28) *with $\gamma = \sqrt{3}$) and the model* (A.1)-(A.2) *are equivalent.*

Corollary A.2. *Consider a modified Green-Naghdi model where the definition* (A.3) *of $\mathcal{R}_2[h, z]$ is replaced by*

$$\widetilde{\mathcal{R}}_2[h, z]f = \frac{1}{2h}\nabla_{x,y}(h^2 f) + \frac{3\beta}{4}f\nabla_{x,y}z,$$

then the model (2.1)-(2.5) *with $\delta = 3/2$ and the model* (A.1)-(A.2) *have exactly the same formulation.*

Proof. [Proof of prop. A.1] The proof of the proposition is very simple in the sense that it only relies on simple computations but these computations are very long.
The dispersive terms in the Green-Naghdi model (A.1)-(A.2) i.e. the complementary terms compared to the classical shallow water system write

$$\mathcal{P}_{gn} = \mu\mathcal{T}[H, z_b] \left(\frac{\partial U}{\partial t} + (U.\nabla_{x,y})U \right) + \mu\mathcal{Q}[H, z_b]U,$$

whereas, for the model (2.1)-(2.5) their expression is given by (for $\delta = 3/2$)

$$\mathcal{P} = \mu \left(\nabla_{x,y}(Hp) + \frac{3\beta}{2} p \nabla_{x,y} z_b \right), \tag{A.4}$$

with p defined by

$$p = \frac{2H}{3} \left(\frac{\partial w}{\partial t} + \mathbf{u}.\nabla_0 w \right), \tag{A.5}$$

and w satisfies

$$2w = -H\nabla_0.\mathbf{u} + \frac{3\beta}{2}\mathbf{u}.\nabla_0 z_b. \tag{A.6}$$

In order to prove the result it remains to insert the expression of w given by Eq. (A.6) into Eq. (A.5) then to insert the obtained expression for p into Eq. (A.4) and finally to check that $\mathcal{P} - \mathcal{P}_{gn} = \mathcal{O}(\mu\beta^2)$ holds true.

Notice that in order to be consistent with the model formulation (A.1)-(A.2), in Eq. (A.4) the value of $\mathcal{P}$ is multiplied by the shallowness parameter μ and the gradient of the topography $\nabla_0 z_b$ is multiplied by β in Eqs. (A.4),(A.6).

Since they can be easily carried out using any symbolic computation software, we do not reproduce the details of the computations allowing to obtain the simplified expression for the quantity $\mathcal{P} - \mathcal{P}_{gn}$ corresponding to

$$\mathcal{P} - \mathcal{P}_{gn} = \frac{\mu\beta^2}{4} \left(\nabla_{x,y} z_b . \Big(\frac{\partial U}{\partial t} + (U.\nabla_{x,y})U \Big) \right) \nabla_{x,y} z_b + \frac{\mu\beta^2}{4} (U.(U.\nabla_{x,y})\nabla_{x,y} z_b) \nabla_{x,y} z_b. \tag{A.7}$$

■

Proof. [Proof of corollary. A.2] The proof is a direct consequence of the expression obtained for $\mathcal{P} - \mathcal{P}_{gn}$ in Eq. (A.7) since we can rewrite

$$\begin{aligned} \mathcal{P} - \mathcal{P}_{gn} = \mu\beta(\mathcal{R}_2[H, z_b] - \widetilde{\mathcal{R}}_2[H, z_b]) \left(\nabla_{x,y} z_b . \Big(\frac{\partial U}{\partial t} + (U.\nabla_{x,y})U \Big) \right) \\ + \mu\beta(\mathcal{R}_2[H, z_b] - \widetilde{\mathcal{R}}_2[H, z_b]) \left(U.(U.\nabla_{x,y})\nabla_{x,y} z_b \right). \end{aligned}$$

■

References

[1] G. B. Airy. Tides and Waves. *Encycl. Metropolitana*, 5:291–369, 1845.

[2] Nora Aïssiouene, Marie-Odile Bristeau, Edwige Godlewski, and Jacques Sainte-Marie. A combined finite volume - finite element scheme for a dispersive shallow water system. *Netw. Heterog. Media*, 11(1):1–27, 2016.

[3] S. Allgeyer, M.-O. Bristeau, D. Froger, R. Hamouda, V. Jauzein, A. Mangeney, J. Sainte-Marie, F. Souillé, and M. Vallée. Numerical approximation of the 3d hydrostatic Navier-Stokes system with free surface. *ESAIM: M2AN*, 53(6):1981–2024, 2019.

[4] B. Alvarez-Samaniego and D. Lannes. Large time existence for 3D water-waves and asymptotics. *Invent. Math.*, 171(3):485–541, 2008.

[5] C. Amante and B. W. Eakins. Etopo1 1 Arc-Minute Global Relief Model: Procedures, Data Sources and Analysis. Research report, National Geophysical Data Center, NOAA, 2009.

[6] E. Audusse, F. Bouchut, M.-O. Bristeau, R. Klein, and B. Perthame. A Fast and Stable Well-Balanced Scheme with Hydrostatic Reconstruction for Shallow Water Flows. *SIAM J. Sci. Comput.*, 25(6):2050–2065, 2004.

[7] E. Audusse and M.-O. Bristeau. A well-balanced positivity preserving second-order scheme for Shallow Water flows on unstructured meshes. *J. Comput. Phys.*, 206(1):311–333, 2005.

[8] Ivo Babuska. The Finite Element Method with Lagrangian Multipliers. *Numer. Math.*, 20:179–192, 1972/73.

[9] A.-J.-C. Barré de Saint-Venant. Théorie du mouvement non permanent des eaux avec applications aux crues des rivières et à l'introduction des marées dans leur lit. *C. R. Math. Acad. Sci. Paris*, 73:147–154, 1871.

[10] Bathymetry & Relief. NOAA home page. https://www.ngdc.noaa.gov/mgg/global/global.html, 2017.

[11] J. Behrens and F. Dias. New computational methods in tsunami science. *Philos Trans A Math Phys Eng Sci.*, Oct 28(373):(2053), 2015.

[12] J.-L. Bona, T.-B. Benjamin, and J.-J. Mahony. Model equations for long waves in nonlinear dispersive systems. *Philos. Trans. Royal Soc. London Series A*, 272:47–78, 1972.

[13] J. L. Bona, M. Chen, and J.-C. Saut. Boussinesq equations and other systems for small-amplitude long waves in nonlinear dispersive media: Part I. Derivation and linear theory. *J. Nonlinear Sci.*, 12:283–318, 2002.

[14] P. Bonneton, E. Barthelemy, F. Chazel, R. Cienfuegos, D. Lannes, F. Marche, and M. Tissier. Recent advances in Serre-Green Naghdi modelling for wave transformation, breaking and runup processes. *European Journal of Mechanics - B/Fluids*, 30(6):589–597, 2011. Special Issue: Nearshore Hydrodynamics.

[15] P. Bonneton, F. Chazel, D. Lannes, F. Marche, and M. Tissier. A splitting approach for the fully nonlinear and weakly dispersive Green-Naghdi model. *J. of Comp. Phys.*, 230(4):1479–1498, 2010.

[16] F. Bouchut. An introduction to finite volume methods for hyperbolic conservation laws. *ESAIM Proc.*, 15:107–127, 2004.

[17] F. Bouchut. *Nonlinear stability of finite volume methods for hyperbolic conservation laws and well-balanced schemes for sources*. Birkhäuser, 2004.

[18] D. Bresch, E. Fernandez-Nieto, I. Ionescu, and P. Vigneaux. Augmented Lagrangian Method and Compressible Visco-Plastic Flows : Applications to Shallow Dense Avalanches. In *New Directions in Mathematical Fluid Mechanics*, Advances in Mathematical Fluid Mechanics, pages 57–89. Birkhäuser, 2010. accepted November 2008. 33 pages. 12 figures.

[19] F. Brezzi. On the existence, uniqueness and approximation of saddle-point problems arising from Lagrangian multipliers. *Rev. Française Automat. Informat. Recherche Opérationnelle Sér. Rouge*, 8(R-2):129–151, 1974.

[20] M-O. Bristeau and B. Coussin. Boundary Conditions for the Shallow Water Equations solved by Kinetic Schemes. Rapport de recherche RR-4282, INRIA, 2001. Projet M3N.

[21] M.-O. Bristeau, A. Mangeney, J. Sainte-Marie, and N. Seguin. An energy-consistent depth-averaged Euler system: Derivation and properties. *Discrete and Continuous Dynamical Systems - Series B*, 20(4):961–988, 2015.

[22] R. Camassa, D. D. Holm, and C. D. Levermore. Long-time effects of bottom topography in shallow water. *Physica D*, 98(2-4):258–286, 1996. Nonlinear phenomena in ocean dynamics (Los Alamos, NM, 1995).

[23] F. Chazel, D. Lannes, and F. Marche. Numerical Simulation of Strongly Nonlinear and Dispersive Waves Using a Green–Naghdi Model. *J. Sci. Comput.*, 48(1-3):105–116, 2011.

[24] A. J. Chorin. Numerical solution of the Navier-Stokes equations. *Math. Comput.*, 22:745–762, 1968.

[25] R. Cienfuegos, E. Barthélemy, and P. Bonneton. A fourth-order compact finite volume scheme for fully nonlinear and weakly dispersive Boussinesq-type equations. Part I: Model development and analysis. *Internat. J. Numer. Methods Fluids*, 51(11):1217–1253, 2006.

[26] Anne-Sophie Bonnet-Ben Dhia, Marie-Odile Bristeau, Edwige Godlewski, Sébastien Imperiale, Anne Mangeney, and Jacques Sainte-Marie. Pseudo-compressibility, dispersive model and acoustic waves in shallow water flows. working paper or preprint, 2020.

[27] M.-W. Dingemans. *Wave propagation over uneven bottoms*. Advanced Series on Ocean Engineering - World Scientific, 1997.

[28] A. Duran and F. Marche. Discontinuous-Galerkin discretization of a new class of Green-Naghdi equations. *Commun. Comput. Phys.*, 17(3):721–760, 2015.

[29] A. Duran and F. Marche. A discontinuous Galerkin method for a new class of Green-Naghdi equations on simplicial unstructured meshes. *Appl. Math. Model.*, 45:840–864, 2017.

[30] A. Ern and J.-L. Guermond. *Theory and Practice of Finite Elements*. Springer, 2004.

[31] C. Escalante, T. Morales, and M.-J. Castro. Weakly dispersive shallow water flows: an efficient implementation using a finite-volume finite-difference scheme. In *Proceedings of the XXIV congress on differential equations and applications XIV congress on applied mathematics*, pages 255–259, 2015.

[32] E. D. Fernandez-Nieto, M. Parisot, Y. Penel, and J. Sainte-Marie. A hierarchy of dispersive layer-averaged approximations of Euler equations for free surface flows. *Commun. Math. Sci.*, 16(5):1169–1202, 2018.

[33] A. G. Filippini, M. Kazolea, and M. Ricchiuto. A flexible genuinely nonlinear approach for nonlinear wave propagation, breaking and run-up. *J. Comp. Phys.*, 310:381–417, 2016.

[34] F. Gallerano, G. Cannata, and M. Villani. An integral contravariant formulation of the fully non-linear Boussinesq equations. *Coastal Engineering*, 83:119–136, 2014.

[35] J.-F. Gerbeau and B. Perthame. Derivation of Viscous Saint-Venant System for Laminar Shallow Water; Numerical Validation. *Discrete Contin. Dyn. Syst.*, 1(1):89–102, 2001.

[36] S. Glimsdal, G. K. Pedersen, C. B. Harbitz, and F. Løvholt. Dispersion of tsunamis: does it really matter? *Natural Hazards and Earth System Sciences*, 13(6):1507–1526, 2013.

[37] E. Godlewski and P.-A. Raviart. *Numerical approximation of hyperbolic systems of conservation laws*. Applied Mathematical Sciences, vol. 118, Springer, New York, 1996.

[38] A. E. Green and P. M. Naghdi. A derivation of equations for wave propagation in water of variable depth. *J. Fluid Mech.*, 78:237–246, 1976.

[39] J-L. Guermond. Some implementations of projection methods for Navier-Stokes equations. *ESAIM, Math. Model. Numer. Anal.*, 30(5):637–667, 1996.

[40] J-L. Guermond and J. Shen. On the error estimates for the rotational pressure-correction projection methods. *Math. Comput.*, 73(248):1719–1737, 2004.

[41] Frédéric Hecht and C. Parés. Nsp1B3 : un logiciel pour résoudre les équations de Navier Stokes incompressible 3D. Research Report RR-1449, INRIA, 1991. Projet MENUSIN.

[42] O. A. Ladyzhenskaya. *The mathematical theory of viscous incompressible flow*. New York: Gordon and Breach, 1969.

[43] D. Lannes. *The water waves problem*, volume 188 of *Mathematical Surveys and Monographs*. American Mathematical Society, 2013. Mathematical analysis and asymptotics.

[44] D. Lannes and F. Marche. A new class of fully nonlinear and weakly dispersive Green-Naghdi models for efficient 2D simulations. *J. Comput. Phys.*, 282:238–268, 2015.

[45] Patrick Lascaux and Raymond Theodor. *Analyse numérique matricielle appliquée à l'art de l'ingénieur*. Masson, 1986.

[46] O. Le Métayer, S. Gavrilyuk, and S. Hank. A numerical scheme for the Green-Naghdi model. *J. Comp. Phys.*, 229(6):2034–2045, 2010.

[47] R.-J. LeVeque. *Finite Volume Methods for Hyperbolic Problems*. Cambridge University Press, 2002.

[48] P.-L. Lions, B. Perthame, and P. E. Souganidis. Existence of entropy solutions to isentropic gas dynamics system. *Commun. Pure Appl. Math.*, 49:599–638, 1996.

[49] P.-L. Lions, B. Perthame, and E. Tadmor. Kinetic formulation of the isentropic gas dynamics and p-systems. *Commun. Math. Physics*, 163:415–431, 1994.

[50] O. Nwogu. Alternative form of Boussinesq equations for nearshore wave propagation. *Journal of Waterway, Port, Coastal and Ocean Engineering, ASCE*, 119(6):618–638, 1993.

[51] D. H. Peregrine. Long waves on a beach. *J. Fluid Mech.*, 27:815–827, 1967.

[52] O. Pironneau. *Méthodes des éléments finis pour les fluides.* Masson, 1988.

[53] R. Rannacher. On Chorin's projection method for the incompressible Navier-Stokes equations. In G. Heywood, John, Kyûya Masuda, Reimund Rautmann, and A. Solonnikov, Vsevolod, editors, *The Navier-Stokes Equations II — Theory and Numerical Methods*, volume 1530 of *Lecture Notes in Mathematics*, pages 167–183. Springer, 1992.

[54] W. C. Thacker. Some exact solutions to the non-linear shallow-water wave equations. *J. Fluid Mech.*, 107:499–508, 1981.

[55] B. Van Leer. Towards the ultimate conservative difference scheme. V. A second-order sequel to Godunov's method. *J. Comput. Phys.*, 135(2):227–248, 1997. With an introduction by Ch. Hirsch, Commemoration of the 30th anniversary {of J. Comput. Phys.}.